



Mitigating systematic error in topographic models for geomorphic change detection: accuracy, precision and considerations beyond off-nadir imagery

Mike R. James,^{1,2*} Gilles Antoniazza,³ Stuart Robson⁴ and Stuart N. Lane³

¹ Lancaster Environment Centre, Lancaster University, Lancaster, UK

² Lancaster Intelligent Robotic & Autonomous Systems Centre, Lancaster University, Lancaster, UK

³ Institute of Earth Surface Dynamics, University of Lausanne, Lausanne, Switzerland

⁴ Department of Civil, Environmental and Geomatic Engineering, University College London, London, UK

Received 9 October 2019; Revised 5 February 2020; Accepted 7 April 2020

*Correspondence to: Mike R. James, Lancaster Environment Centre, Lancaster University, Lancaster LA1 4YQ, UK. E-mail: m.james@lancaster.ac.uk

This is an open access article under the terms of the Creative Commons Attribution License, which permits use, distribution and reproduction in any medium, provided the original work is properly cited.

ESPL

Earth Surface Processes and Landforms

ABSTRACT: Unmanned aerial vehicles (UAVs) and structure-from-motion photogrammetry enable detailed quantification of geomorphic change. However, rigorous precision-based change detection can be compromised by survey accuracy problems producing systematic topographic error (e.g. ‘doming’), with error magnitudes greatly exceeding precision estimates. Here, we assess survey sensitivity to systematic error, directly correcting topographic data so that error magnitudes align more closely with precision estimates. By simulating conventional grid-style photogrammetric aerial surveys, we quantify the underlying relationships between survey accuracy, camera model parameters, camera inclination, tie point matching precision and topographic relief, and demonstrate a relative insensitivity to image overlap. We show that a current doming-mitigation strategy of using a gently inclined (<15°) camera can reduce accuracy by promoting a previously unconsidered correlation between decentring camera lens distortion parameters and the radial terms known to be responsible for systematic topographic error. This issue is particularly relevant for the wide-angle cameras often integrated into current-generation, accessible UAV systems, frequently used in geomorphic research. Such systems usually perform on-board image pre-processing, including applying generic lens distortion corrections, that subsequently alter parameter interrelationships in photogrammetric processing (e.g. partially correcting radial distortion, which increases the relative importance of decentring distortion in output images). Surveys from two proglacial forefields (Arolla region, Switzerland) showed that results from lower-relief topography with a 10°-inclined camera developed vertical systematic doming errors > 0.3 m, representing accuracy issues an order of magnitude greater than precision-based error estimates. For higher-relief topography, and for nadir-imaging surveys of the lower-relief topography, systematic error was < 0.09 m. Modelling and subtracting the systematic error directly from the topographic data successfully reduced error magnitudes to values consistent with twice the estimated precision. Thus, topographic correction can provide a more robust approach to uncertainty-based detection of event-scale geomorphic change than designing surveys with small off-nadir camera inclinations and, furthermore, can substantially reduce ground control requirements. © 2020 The Authors. Earth Surface Processes and Landforms published by John Wiley & Sons Ltd

KEYWORDS: UAV; DEM; structure-from-motion; systematic doming error; decentring lens distortion; topographic correction

Introduction

The use of unmanned aerial vehicles (UAVs) has become an established approach for acquiring centimetre-resolution topographic information through structure-from-motion (SfM) photogrammetry (e.g. Eltner et al., 2015; Harwin and Lucieer, 2012; Hugenholtz et al., 2013; Niethammer et al., 2010; Ouedraogo et al., 2014; Rosnell and Honkavaara, 2012; Turner et al., 2015). Challenges remain in forecasting the achievable accuracy of output topographic data during project planning, where, here, we specifically

distinguish between the measurement ‘accuracy’ (associated with systematic error or bias) and ‘precision’ (describing random error). In order to use rigorous techniques for successful geomorphic change detection (such as M3C2-PM; James et al., 2017b; Lague et al., 2013), accuracy issues must be substantially smaller than the precision estimates used to determine the detectable magnitude of change for a particular confidence level. Although spatially variable precision estimates can be made for individual surveys (Dall’Asta et al., 2015; James et al., 2017b), no reliable and generalized method exists to predict the likely magnitude of systematic errors such as

topographic doming, that affect the accuracy of the output topographic data. Typically, improving accuracy through mitigation of systematic error currently requires time-consuming independent measurements [e.g. the deployment and measurement of ground control points (GCPs) or Global Navigation Satellite System (GNSS) profiles], specific survey designs or the use of more costly UAVs with on-board GNSS suitable for providing camera position data to decimetric accuracy.

Accuracy issues in blocks of photogrammetric images from UAV topographic surveys are often due to systematic errors in the camera geometric model estimated during photogrammetric processing (e.g. Hastedt and Luhmann, 2015). These errors arise due to the typically relatively weak image network geometry, combined with correlations between the photogrammetric parameters that estimate camera poses and internal imaging geometry. Such issues result in a complex set of local optimization minima to which the processing can converge (i.e. during bundle adjustment), rather than a well-defined minimum that would result from a highly convergent multi-image network used for camera calibration or industrial measurement (e.g. Fraser, 2001, 2013). The situation is further influenced by the developing trend of manufacturers integrating 'geometric lens correction' pre-processing on-board cameras. With such on-board lens distortion corrections being generic (i.e. derived for a specified camera/lens make and model, but not tailored to the manufacturing and deployment variations of each individual camera), they cannot provide the sub-pixel accuracy required for detailed geomorphic change detection. Furthermore, the characteristics of the residual image distortion, after 'black-box' on-board corrections have been applied, may result in an output image geometry that, at best, alters the significance of each of the optical-physics-based parameters that typically underpin distortion modelling in widely-used photogrammetric software and, at worst, cannot be corrected by the largely radial geometries described by such parameters. Consequently, photogrammetric processing of pre-processed imagery may be susceptible to unanticipated parameter interactions within physically-based distortion models, which could influence the accuracy of topographic results.

Here, we characterize a previously unexplored interaction between estimated decentring and radial lens distortion parameters that can result in systematic error in surveys specifically designed to mitigate topographic doming. Whereas previous work has focussed on doming mitigation through improving the camera model (Carbonneau and Dietrich, 2017; James and Robson, 2014a; Wackrow and Chandler, 2011), we demonstrate an alternative approach, in which systematic topographic error is modelled and removed directly from results, thus minimizing bias and aligning error magnitudes more closely to those expected from precision estimates. In example surveys of proglacial forefields, we show that this method can support the robust quantification of geomorphic change through enhancing the level of detection by up to an order of magnitude.

Background to the Study

Systematic topographic error and radial lens distortion

Systematic 'doming error' is a widely recognized difficulty in UAV-based topographic surveying, and results from error in radial lens distortion estimates in camera models being correlated with, and inseparable from, systematic Z-error in surface shape (Fryer and Mitchell, 1987; Wackrow and Chandler, 2008, 2011). Previous work has demonstrated that image sets with

near-parallel viewing directions are particularly susceptible, due to difficulties in accurately estimating the radial lens distortion in self-calibrating bundle adjustments for this image network geometry (Fryer and Mitchell, 1987; Wackrow and Chandler, 2008, 2011). Doming can be mitigated by strengthening the image network through using a convergent imaging geometry, and simulations suggest that effective mitigation can be possible for relatively small camera inclination angles from nadir (e.g. 5°–10°; James and Robson, 2014a). However, field-based examples have shown that the advantages of such small-angle convergences do not always transfer effectively to practical surveys (Nesbit and Hugenholtz, 2019).

Radial distortion is the main geometric optical effect in raw imagery and, based on this, previous work to understand systematic topographic error has considered only radial distortion components. For raw imagery, magnitudes of radial distortion in wide-angle cameras are up to tens to hundreds of pixels (e.g. Brown, 1971; Clarke and Fryer, 1998; Fryer and Brown, 1986; Krauss, 2007; Luhmann et al., 2014, 2016; Robson and Shortis, 1998; Robson et al., 1999). In contrast (and for well-manufactured optical systems), other distortions such as decentring typically amount to less than 10 pixels. For example, our previous laboratory calibrations of digital Single Lens Reflex (dSLR) cameras and 28mm lenses for ground-based topographic work (e.g. James et al., 2007; James and Robson, 2014b; James et al., 2006) have shown maximum decentring distortion magnitudes of < 0.5 pixels, around two orders of magnitude smaller than those from radial parameters (~50 pixels). At such magnitudes, decentring components can sometimes be removed from the distortion model because the parameter values cannot be determined as significantly different from zero during calibration (i.e. parameter value magnitudes that do not exceed their measurement precision; e.g. Fraser, 2001; Gruen and Beyer, 2001).

In-camera image pre-processing

A complication with widely used cameras such as the DJI Phantom 4 Pro quadcopter's FC6310, is that, under default settings, the imagery has already undergone some manufacturer-specific geometric adjustments on board the camera as part of a pre-processing conversion of raw image data, for export as JPEG-format image files (Figure 1; e.g. Cramer et al., 2017; O'Connor et al., 2017; Peppas et al., 2019). These on-board adjustments are designed to reduce the visual geometric artefacts (e.g. straight lines appearing curved) that result from the dominant radial distortion in raw imagery, and may be based on a generic understanding of the geometric distortions of the lens type fitted to the camera. With wide angle cameras, these corrections can also include image cropping as the images are radially expanded to correct for image curvature. Comparing FC6310 raw image data with their associated JPEG images, for example, suggests that radial corrections of up to ~500 pixels have been applied on-board the camera prior to output as JPEG-format images (Figure 1). Additional processing, such as increasing sharpness, colour space adjustments and changes in image tonality are also typically carried out at this stage, but are not anticipated to have a significant effect on image geometry when compared to the optical distortion.

Hence, for such pre-processed JPEG images, an initial radial geometric correction has already been carried out. Consequently, in subsequent SfM-photogrammetry workflows, caution should be exercised with the assumption of image distortion being dominantly radial (which, until recently, could be broadly applied); derived lens distortion estimates will describe corrections to previously applied corrections, rather than

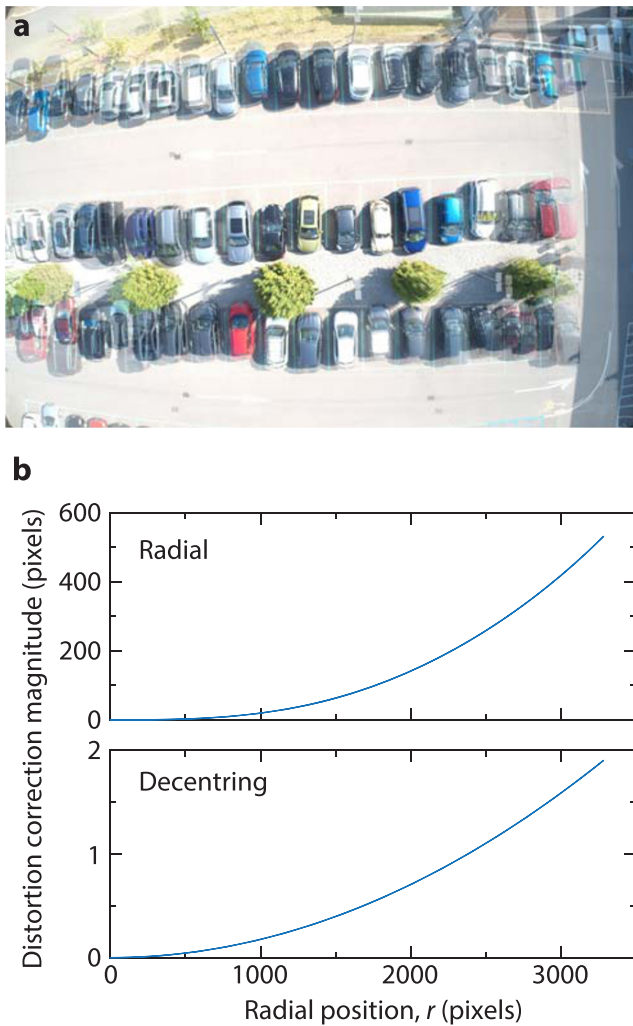


FIGURE 1. On-board geometric corrections applied by a DJI FC6310 camera during image pre-processing prior to output as JPEG. (a) Raw image (5464×3640 pixels, saved as a DNG-format file) overlain by the equivalent image output from the camera as a JPEG (5472×3648 pixels, with 60% transparency). (b) Distortion profiles for the best-fit camera model that relates the JPEG output to the raw image and represent the manufacturer-applied geometric corrections (based on ~ 8200 tie points matched across the images in Agisoft Metashape v.1.5.0, using three radial and two decentering distortion parameters, giving a root mean square (RMS) residual of 0.15 pixels). The magnitude of decentering corrections are illustrated through the profile function (Fraser, 2001), $P(r) = (P_1^2 + P_2^2)^{1/2} r^2$. [Colour figure can be viewed at wileyonlinelibrary.com]

actual lens distortion displacements. For JPEGs from the DJI systems used in our fieldwork here, modelled radial corrections at the image extremities were a similar order of magnitude (in pixels) to those seen in our dSLRs previously used for ground-based work (e.g. 20–50 pixels). In contrast, decentering displacements in the DJI systems were approximately an order of magnitude larger (i.e. ~ 4 pixels) than in the dSLRs. Consequently, for JPEG-format image output from such cameras, modelling of decentering distortion is likely to be critical for accurate results, and the influence of decentering parameters on systematic topographic error needs to be assessed.

Decentering distortion

In photogrammetry, the almost ubiquitous approach to representing image distortion in consumer cameras is through models based on the optical physics of camera lens systems.

The Brown–Conrady distortion model (Brown, 1966) is the most commonly used of such physically-based models, and includes decentering parameters, P_1 and P_2 , that describe displacements (dx , dy) at image coordinates x and y , with both radial and tangential components:

$$dx = P_1(r^2 + 2x^2) + 2P_2xy \quad (1)$$

$$dy = P_2(r^2 + 2y^2) + 2P_1xy \quad (2)$$

where $r^2 = x^2 + y^2$. Unlike radial corrections, decentering image displacements have components with consistent direction across the image (Figure 2) and, thus, can be susceptible to high correlation with the principal point position during bundle adjustment. However, such correlations and error in decentering parameters may not necessarily result in systematic topographic error; for the weak network geometries typical of aerial surveys, parameter correlation can enable compensation of decentering error through error propagation into estimated camera positions, orientations or principal point coordinates (e.g. Figure 3; Brown, 1966; Fraser, 2001; Fraser, 1997; Fraser, 2013). In particular, decentering distortion has been previously shown to be correlated with camera inclination (Brown, 1966) and, consequently, could influence existing strategies aimed at mitigating topographic doming through using an inclined camera.

Study Aims

In order to maximize SfM survey capabilities for geomorphic studies, accuracy issues (reflecting systematic error) must be minimized so that precision estimates can be used to reliably define appropriate levels of change detection. Motivated by this, and by the increasingly widespread use of complex lenses and internal digital image correction processing in small UAVs, the aims of this article are (i) to quantify the sensitivity of systematic topographic doming error to survey characteristics and expose the relationship to decentering lens parameters, and (ii) to demonstrate how surface change detection can be generically enhanced through successful modelling and removal of systematic topographic error. We initially use simulated UAV survey data, processed within established photogrammetric and SfM-based software to identify and to explore the relationships between the mitigation of systematic error and decentering lens parameters. The simulations enable us to quantify the sensitivity of topographic accuracy to survey characteristics such as precision of image feature localization, image overlap and topographic relief. We then use these results to interpret the error characteristics of proglacial forefield surveys carried out with DJI FC6310 cameras that output default JPEG-format imagery. Finally, we demonstrate the effectiveness of modelling and directly removing systematic error from the resulting topographic data, to enable event-level geomorphic change detection through using effective, spatially variable, precision-based levels of detection.

Methods: Quantifying Survey Sensitivities to Systematic Error

The simulation-based components of our work were designed (i) to identify the effects of decentering lens distortion parameters on error in topographic data and to determine the interactions involved, and (ii) to quantify survey sensitivity to such

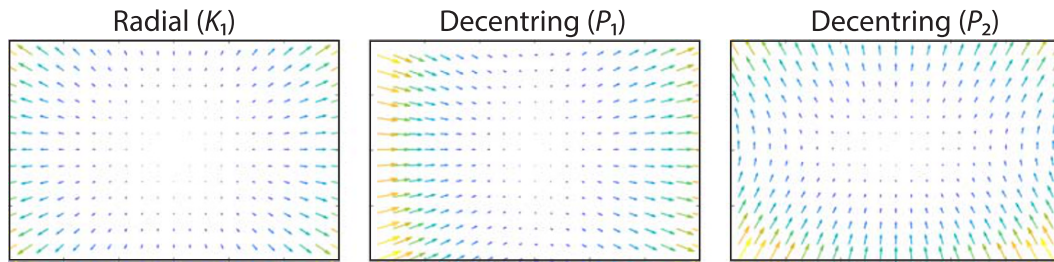


FIGURE 2. Schematic illustration of image coordinate displacements due to radial (K_1) and decentring (P_1 and P_2) parameters in a Brown–Conrady lens distortion model. Note that the relative scaling between the panels is arbitrary (for real lenses radial distortion magnitudes are typically an order of magnitude greater than those of decentring), and that P_1 and P_2 are typically used together, not in isolation, within a camera model. [Colour figure can be viewed at wileyonlinelibrary.com]

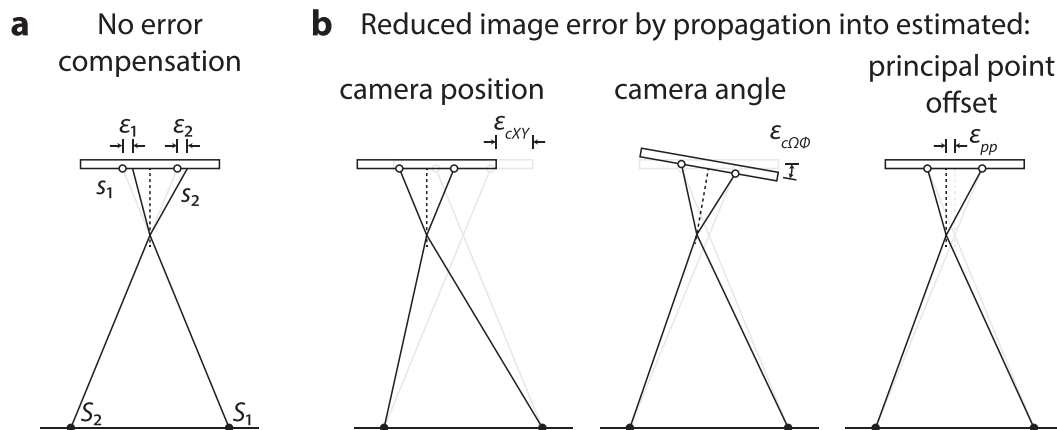


FIGURE 3. Compensation of camera model decentring distortion error. (a) Two topographic points, S_1 and S_2 , are observed in a distortion-free camera at image points s_1 and s_2 (circles), as illustrated by the grey rays. A camera model with error in decentring lens distortion (illustrated by the black rays), gives estimated image projections with associated errors of ϵ_1 and ϵ_2 . (b) These errors in image space can be reduced by propagating error into the estimated camera position, orientation or principal point offset (compare the black rays and outlines with the error-free equivalents in grey).

systematic error. We generated simulated photogrammetric image networks based on established aerial survey protocols to represent UAV surveys, with parallel, overlapping image strips connected into image blocks. A nominal image network design was constructed from which variants were then explored to assess sensitivities to survey characteristics. Although the simulation approach is scale-independent, to facilitate familiarity, our nominal survey was constructed at a spatial scale relevant to geomorphological studies (e.g. with centimetric ground sampling distances (GSDs) acquired from a flight height of 50 m, over areas with dimensions of hundreds of metres; Table 1).

The nominal survey comprised 48 images in two orthogonal blocks (a ‘double-grid’) of four parallel strips (six images in each strip), with along- and cross-strip overlaps of 80% reflecting the strong image overlap typically used with UAV data collection (e.g. Eltner et al., 2015; Rosnell and Honkavaara, 2012; Woodget et al., 2015). A grid of virtual three-dimensional (3D) tie points represented the topographic surface, for which simulated tie point image observations were calculated to construct the photogrammetric network. To represent the finite precision of tie point image measurements (i.e. to reflect noise in tie point image coordinates), pseudo-random offsets (selected from a normal distribution with a 0.5-pixel standard deviation) were added to the tie point image coordinate values.

Photogrammetric estimates of the 3D tie point coordinates were initially determined by intersection, and then image networks were processed by self-calibrating bundle adjustment in either close range photogrammetry software, VMS (Vision Measurement System v.8.72, <http://www.geomsoft.com>), or PhotoScan v.1.4.3 (now Metashape; <http://www.agisoft.com>), as detailed later. The simulations thus represent synthetic data processed with the same algorithms as real image networks.

In order to focus on systematic error within the image networks, control data (e.g. GCPs) were not used and, following bundle adjustment, the tie point cloud was realigned for a least-squares best-fit with its initial position estimates, through a 3D translation and rotation.

For each 3D tie point, topographic Z-error was determined as the Z-coordinate change with respect to the initial intersection value. Systematic doming-related error was then characterized by the difference between the mean vertical error on points within a 5-m horizontal distance of the survey centre (approximately 75 points), and those within 2.5 m of a radial distance of 40 m of the centre (approximately 1250 points; the simulations represented a surface extent of $\sim 80 \text{ m} \times 80 \text{ m}$).

Due to the correct camera orientations being pre-defined within the simulation approach, we could also determine the error in the output camera orientations estimated by the bundle adjustment. To detect any systematic error components in estimated camera position, ϵ_{cXYZ} and camera pointing direction, $\epsilon_{c\Omega\phi\kappa}$, camera orientation errors were fitted with models parameterized by camera position:

$$\epsilon_{cXYZ} = \begin{bmatrix} a_x \\ a_y \\ a_z \end{bmatrix} + \begin{bmatrix} b_x \\ b_y \\ b_z \end{bmatrix} X' + \begin{bmatrix} c_x \\ c_y \\ c_z \end{bmatrix} Y' + \begin{bmatrix} d_x \\ d_y \\ d_z \end{bmatrix} R^2 \quad (3)$$

$$\epsilon_{c\Omega\phi\kappa} = \begin{bmatrix} a_\Omega \\ a_\phi \\ a_\kappa \end{bmatrix} + \begin{bmatrix} b_\Omega \\ b_\phi \\ b_\kappa \end{bmatrix} X' + \begin{bmatrix} c_\Omega \\ c_\phi \\ c_\kappa \end{bmatrix} Y' \quad (4)$$

where X' and Y' are the horizontal coordinates of a camera

Table 1. Characteristics of the survey simulations

	Simulation value
<i>Camera</i>	
Focal length (F , mm)	20
Image size (pixels)	4000 × 3000
Pixel pitch (μm)	5.0
<i>Nominal survey specifications</i>	
Flight height (m)	50
Image footprint (m)	50.0 × 37.5
Ground sampling distance (mm)	12.5
Imaging direction	nadir, with pseudo-random perturbations in roll, pitch and yaw (standard deviation 1°)
Image network design	48 images in total: two image blocks overlapping at 90°; each block comprises four image strips, of six images each
Image overlap (along-strip, cross-strip; %)	80, 80
<i>Tie point features</i>	
Density on the ground (features per m^2)	1
Total number observed in survey	~60000
Number observed in one image	~1870
Precision of image observations (pixels)	0.50
<i>Simulation variants</i>	
Camera models (a–d): ^a optimized lens distortion parameters	(a) $C_x, C_y, B_1, B_2, K_1, K_2, K_3, P_1, P_2$
Camera mean forward inclination (deg)	(b) $C_x, C_y, B_1, B_2, K_1, K_2, K_3, P_1$ (c) K_1, P_2 (d) K_1 0, 5, 10 and 15

^aPrincipal point offset (C_x, C_y), radial distortion (K_{1-3}), decentring distortion ($P_{1,2}$), and affinity and orthogonality ($B_{1,2}$). Focal length (principal distance) was also free to vary within bundle adjustments.

from the centroid of the tie points, $R = (X'^2 + Y'^2)^{1/2}$ and is the radial distance from the centroid, and vectors a, b, c and d contain the adjusted model parameters.

Identifying the influence of decentring distortion

The relationships between systematic surface error, decentring distortion, and camera inclination, were assessed through simulations based on variants of the nominal survey (Table 1) processed by self-calibrating bundle adjustment using VMS. The survey variants differed by including different combinations of distortion parameters, some with fixed error, and by repeating simulations with a mean camera inclination of 5° from nadir, either forward (i.e. in pitch) or to the side (roll). To assess the repeatability of results, some simulations were carried out five times, each time with a different set of pseudo-random offsets added to the tie point image observations. Other simulations were also carried out with the image observation offsets taken from a normal distribution of 0.6-pixel standard deviation (cf. 0.5 pixels as used generally; Table 1), in order to enhance doming and hence improve the likelihood of detecting subtle systematics within the associated camera position errors.

Systematic topographic error and survey characteristics

To explore the sensitivity of systematic topographic error to survey characteristics such as tie point image measurement precision, image overlap, and topographic relief (which gives variations in viewing distance), subsequent simulations were processed via batch processing (unavailable in VMS) in PhotoScan. However, PhotoScan only optimized camera parameters when 3D tie points were not co-planar, thus, for PhotoScan-processed simulations, the nominal survey (Table 1) was modified by adding pseudo-random vertical offsets (from a

normal distribution with standard deviation of 1 m) to the virtual 3D tie point positions.

The batch processing used a Python script to vary survey characteristics, add pseudo-random offsets, carry out the bundle adjustments and export results for repeated simulations. This approach enabled us to not only add different pseudo-random offsets to the image observations, but also to the camera orientations (by default, taken from normal distributions of 0.5 pixel and 1° standard deviations, respectively). Consequently, any specific survey scenario was used for 200 simulations, each one with different pseudo-random perturbations to camera orientations and to image observations.

Simulations were carried out with cameras of mean forward inclinations of 0° (i.e. nadir), 5°, 10° and 15°. To highlight the influence of estimating decentring distortion, each scenario was explored using four different camera models (a–d; Table 1) that contained either many (a, b) or few (c, d) distortion parameters to be estimated, and either included (a, c) or excluded (b, d) the decentring parameter P_2 . For all combinations of camera model and mean forward inclination, we explored doming sensitivity (i) to the magnitude of tie point image measurement precision (0.1–1.0 pixels), (ii) to image overlap (50–90%), and to topographic variability (i.e. magnitudes of topographic relief) over either (iii) within-image spatial scales or (iv) survey-wide (giving a total of >86 000 bundle adjustments). To change the magnitude of topographic relief represented over within-image spatial scales, the vertical offsets applied to the 3D tie point positions were taken from normal distributions of different standard deviations (between 1 and 10 m, representing 2–20% of the nominal flight height). To consider survey-wide variations in topographic relief (i.e. over inter-image or survey scales), additional, systematic offsets were applied to represent topographic slopes of up to ~30° (giving maximum variations of ~40 to 60 m in above-ground flight height across the survey, representing approximately $\pm 20\%$ of the mean flight height).

Methods: Correcting Systematic Topographic Error in Field Surveys

We demonstrate the implications of the simulation results and derive a direct correction approach to topographic doming error using field surveys of proglacial forefields in the Arolla region, Switzerland. Two topographically-contrasting survey areas were considered: a relatively flat region of dominantly dry river bed of la Borgne d'Arolla, with topographic relief of ~14 m (over a survey area of ~50 m × 250 m), and a steeper region of relict moraines from the Tsijiore Nouve glacier, covering a topographic relief of ~85 m (over a survey area of ~100 m × 200 m). Repeat surveys were carried out using a different DJI Phantom 4 Pro quadcopter for each area, with flight plans implemented through Pix4Dcapture (v.4.2). We present results from six surveys of la Borgne d'Arolla, carried out at nominally constant altitudes representing ~30, 60 and 90 m above the take-off point, and six surveys of Tsijiore Nouve, all carried out at a nominal altitude of 60 m above the take-off point. At both sites, three of the surveys were carried out with the camera at nadir and the other three with the camera inclined forward at 10° (for all images). All surveys had a 'double-grid' design of orthogonal flight lines; however, for a nadir camera, Pix4Dcapture only allowed single-grid missions, so the double-grid surveys were implemented through combining two orthogonal single-grid missions (at Tsijiore Nouve, these were carried out without landing between missions). For each flight, the survey extent was identified manually within Pix4Dcapture in the field, resulting in some variation between the number of images acquired by the flight planning software for repeat surveys. To replicate the approach commonly used in geomorphic research, images were output in JPEG format (5472 × 3648 pixels). With a nominal focal length of 8.8 mm and pixel pitch of ~2.4 μm, the integrated FC6310 camera provided ground sampling distances of ~8 to 25 mm. Image acquisition used a global shutter, and automatic exposure settings were set to -2/3 stop to help reduce saturation of reflective ground control targets. Further survey details are provided in Supporting Information Tables S1 and S2, and the associated imagery are freely available at <https://doi.org/10.6084/m9.figshare.c.4677293>.

Photogrammetric control was designed for optimum observation from a distance of 60 m, and implemented using 40 circular targets (DVD discs with a diameter of 0.15 m) mounted on rectangular black boards (~0.4 m × 0.4 m). The targets were distributed across each area, with a small number having to be disregarded within the processing due to being on unstable ground or covered by sediment deposition before being imaged. Target coordinates were measured by total station (la Borgne d'Arolla) or by GNSS (Tsijiore Nouve) and provided in the Swiss CH1903/LV03 system to mean horizontal and vertical precisions of 9 and 17 mm, respectively, for la Borgne d'Arolla, and to 16 and 20 mm for Tsijiore Nouve.

SfM photogrammetric processing

Images for all surveys were processed in PhotoScan v.1.3.4 following Stages I–II (tie point processing, camera self-calibration and quality checks) of James et al. (2017a). Images that were blurred, had poorly distributed or fewer than ~1000 tie point observations, or showed anomalously large tie point residual magnitudes were discarded (see Table S1 for a summary). Different camera models were explored, with focal length, principal point offset, fourradial and two decentring parameters optimized within all models. The more complex topography

of Tsijiore Nouve strengthened the geometry of the image networks, enabling affinity and non-orthogonality parameters also to be assessed [i.e. representing the full model (a) used in the simulations; Table 1]. Image observations of the control targets were made using the manually guided marker image matching in PhotoScan, with all automated observations subsequently verified visually and by checking for outlier image observation residuals.

In PhotoScan's bundle adjustment, 'projection accuracy' settings weight the image observations of tie point and markers, and Agisoft have recommended retaining the default settings values (1.0 pixels for tie points and 0.1 pixels for control point markers; A. Pasmansky, <https://www.agisoft.com/forum/index.php?topic=10852.msg49211#msg49211>). However, our experience is that such values over-weight the control measurements because they typically result in a non-unity standard error of unit weight, σ_0 , for bundle adjustment (σ_0 values are provided in the console pane). Whilst noting that the interpretation of σ_0 is complicated by the software's individual scale-based weighting of tie point observations, a non-unity value conventionally indicates that initial quality estimates are not consistent with the a posteriori error, i.e. error in the results is not in line with the initial estimates of precision. In cases with strong systematic error, over-weighting of control may be a useful practical approach to reduce survey-wide systematic error components, albeit with the risk of introducing other surface artefacts (e.g. see Figure 1 of James et al., 2017a). Consequently, here, we preferred to use tie point projection accuracy values that resulted in $\sigma_0 = 1.00$. Critically, such settings values resulted in point coordinate precision estimates that aligned well with benchmark values derived from VMS (see next section). Note that the aims of our work here do not include exploring settings values in PhotoScan to optimize survey accuracy and we focus on the implications of decentring distortion and on mitigating any doming that does occur, directly in topographic data.

For inter-survey topographic comparisons, a dense point cloud was generated from each survey. Assessing the effects of systematic error correction did not require extensive surface detail so surveys performed at a nominal flight height of 60 m were processed using the 'Medium quality' setting in PhotoScan. The 'Low' and 'High' quality settings values were then used for the 30- and 60-m-flight-height surveys respectively, to minimize differences in point cloud density across the results.

Precision estimates

To derive point coordinate precision estimates for level of detection analysis during inter-survey comparisons, the processed surveys were re-optimized within a recent version of PhotoScan (v.1.5.0, renamed Metashape) that can provide precision estimates directly from the bundle adjustment. This approach generates estimates on timescales of a few seconds, which is much faster than the multiple hours generally required for previous Monte Carlo-based methods (James et al., 2017b). Such estimates are for the sparse point cloud, and were exported to text file by Python script. The estimates were validated by comparison with benchmark precision estimates from VMS and, when derived from a bundle adjustment with 'accuracy' settings that resulted in $\sigma_0 = 1.00$, differences were within 20% (compared to within ~70% when using default accuracy settings). CloudCompare (cloudcompare.org) was then used to interpolate the sparse point cloud 3D precision estimates across the dense point clouds, using a median filter with 2.5-m radius. We provide the Python script to export precision

estimates, and the associated workflow and a summary of the validation using VMS, within the Supporting Information (Code S2 and Workflow S2, respectively).

Accuracy assessment and systematic error correction

Under the assumption of dominantly vertical error, we focussed on GCP Z -error (i.e. the mismatch between photogrammetrically-estimated GCP Z -coordinates and the equivalent ground survey measurements), and considered the root mean square Z error, $RMSE_Z$, separately for control and check points, as indicative metrics of survey performance. The propensity for error within the survey image networks alone (i.e. without using GCPs as control measurements in the bundle adjustment) was determined by initially using GCPs only to scale, rotate and translate the photogrammetric models to the geographic coordinate system. We then assessed the error reduction as the number of control measurements within the bundle adjustment were incrementally increased within a Monte Carlo framework (James et al., 2017a).

To identify systematic error components, the individual vertical GCP errors (Step 1, Figure 4) were fit with a model of systematic vertical error, ε_z (Step 2, Figure 4):

$$\varepsilon_z = a + bX' + cY' + dR^2 \quad (5)$$

where X' , Y' and R are horizontal distances from the centroid of the tie points (as for Equations 3 and 4) and a , b , c and d are the adjusted parameters, representing a constant vertical offset, planar tilts (the linear terms) and doming (the squared radial term, e.g. Carbonneau and Dietrich, 2017), respectively. The magnitude of ε_z and the model residuals thus represent the accuracy (i.e. bias modellable with Equation 5) and precision components of GCP error, respectively. Having parameterized the systematic error model from discrepancies on GCPs, Equation 5

could then be applied as a survey-wide correction to dense point clouds to provide bias-corrected topographic data for inter-survey comparisons (Step 3, Figures 4, 5).

Inter-survey comparisons

Inter-survey comparisons of 3D dense point cloud outputs provide the most direct insight into survey-wide repeatability relevant to geomorphic assessments. We used the uncertainty-bounded M3C2-PM cloud-to-cloud comparison method (James et al., 2017b; Lague et al., 2013) that identifies statistically significant change where differences exceed a spatially varying precision-based level of detection. In the native M3C2 algorithm (Lague et al., 2013), measurement precision is estimated from local apparent roughness, but the M3C2-PM variant (James et al., 2017b) uses externally-sourced point coordinate precision estimates, such as from photogrammetric bundle adjustment (as derived earlier) and, hence, should be used for SfM-derived point clouds (where roughness can be a poor measure of precision).

Inter-survey comparisons were carried out against 'best case' reference point clouds derived from the 60-m nadir survey for la Borgne d'Arolla, and from the nadir survey determined to be least affected by systematic error for Tsijiore Nouve. The reference point clouds were generated by reprocessing the selected surveys using all GCPs as control measurements in the bundle adjustment, repeating the dense image matching, and recalculating the precision estimates.

In many practical cases, adjustment-based precision estimates can be optimistic, so we explored the change detected when using an effective precision, $k\sigma$, where k is a scalar multiplier of the initially estimated 3D precision, σ . With this, the level of detection for a confidence interval of 95%, $LoD_{95\%}$ (Brasington et al., 2003; Brasington et al., 2000; Lane et al., 2003), is then given by

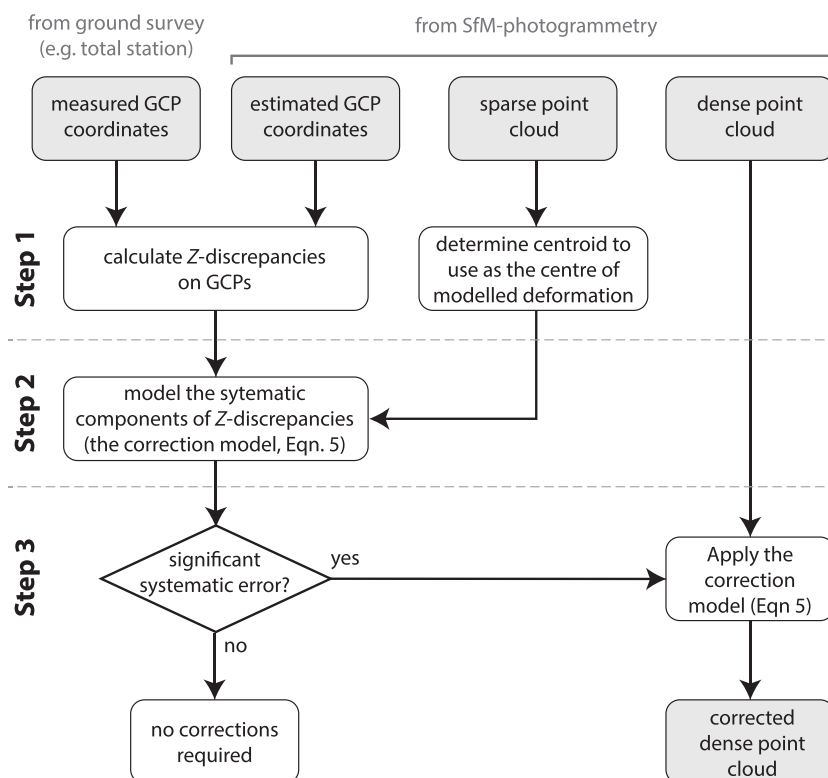


FIGURE 4. Summary workflow for detection and removal of modelled systematic topographic error from SfM surveys.

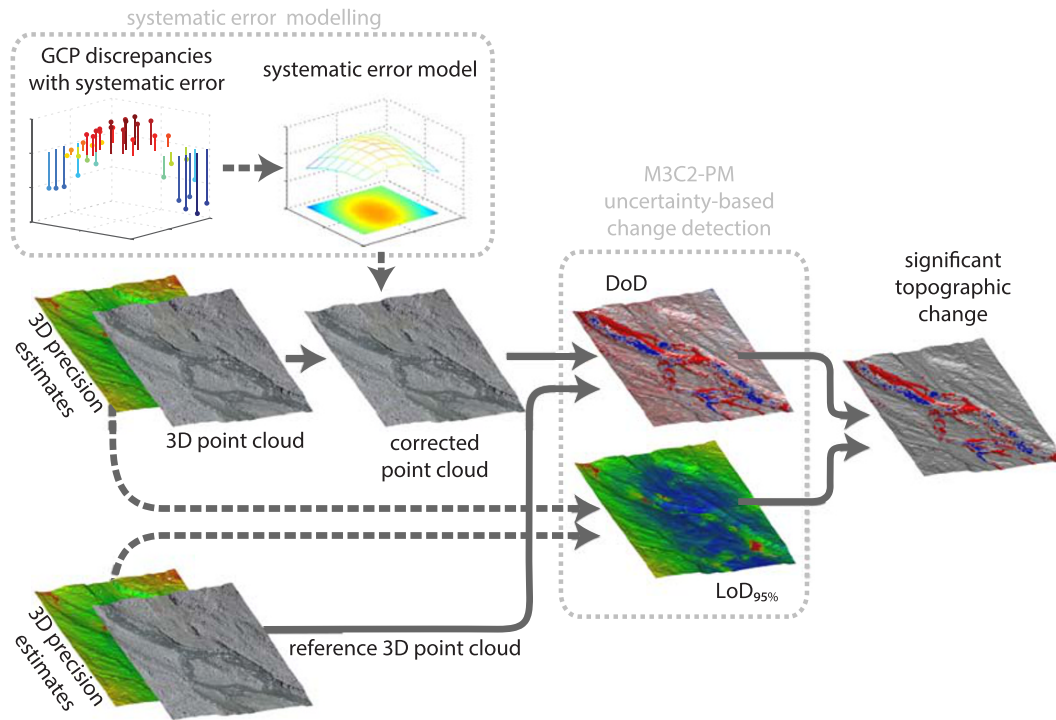


FIGURE 5. Workflow for using systematic topographic error removal to enhance precision-based change detection. [Colour figure can be viewed at wileyonlinelibrary.com]

$$\text{LoD}_{95\%} = 1.96 \left((k\sigma_1)^2 + (k\sigma_2)^2 \right)^{1/2} \quad (6)$$

where subscripts 1 and 2 denote the different surveys. Consequently, if Metashape precision estimates were suitable estimates of point coordinate precision, and accuracy issues had been appropriately removed, then 95% of points in repeat surveys were expected to lie within $\text{LoD}_{95\%}$ for $k = 1$, with differences randomly distributed across the survey area.

Results

Decentering distortion and systematic surface error

The simulations enabled us to explore interactions between decentering distortion and systematic topographic error under

conditions that were free from any of the complexities of field imagery, including those that may result from on-board image pre-processing and resampling. When only the K_1 radial distortion parameter was free to vary within the VMS-processed simulations, the results followed established understanding of topographic doming: with a nadir-oriented camera (perturbed only by small pseudo-random offsets in pointing direction for each photograph), detectable surface doming developed, with an amplitude that correlated with the error in the estimated K_1 value (Figure 6a, filled black symbols; Table 2). This doming was effectively mitigated if the camera had a mean pitch of 5° to give convergence between overlapping flight lines (Figure 6a, filled grey symbols).

However, if decentering distortion parameters were also free to vary within the bundle adjustment, then the doming-mitigation effect of camera inclination was substantially reduced, and dome amplitudes (and K_1 error) were similar to those from the nadir case (Figure 6a, open grey and black

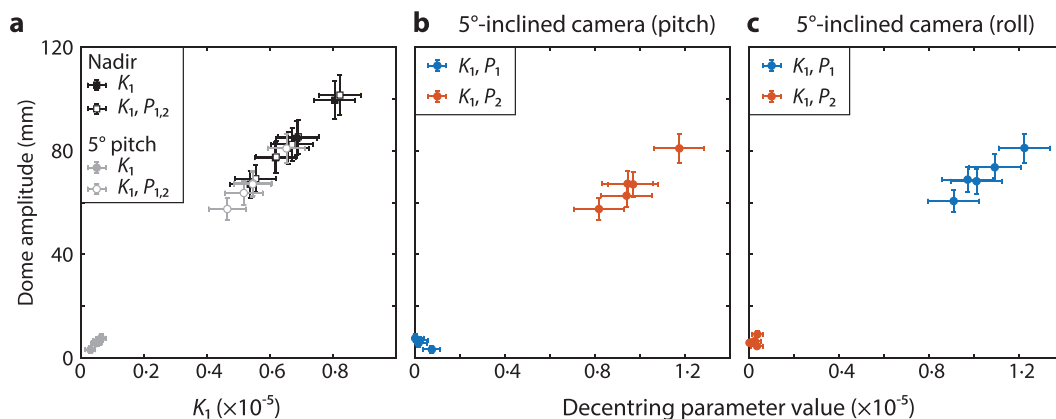


FIGURE 6. Reduction of doming error mitigation by estimating decentering parameters in simulated surveys (Table 1) processed with VMS. Each symbol gives the results of a bundle adjustment of one simulated survey, with error bars representing precision estimates. (a) Doming amplitude versus estimated K_1 value, for surveys with either a nadir or 5° -inclined camera, processed with different distortion parameters sets in the bundle adjustment (either only radial, K_1 , or radial and decentering, $K_1, P_{1,2}$). The differing effects of estimating individual decentering parameters when the camera inclination is in either pitch (b) or in roll (c). [Colour figure can be viewed at wileyonlinelibrary.com]

Table 2. Relationships between systematic error in the modelled topographic surface (doming amplitude), un-modelled camera position error and camera lens distortion parameter values. The nadir- and inclined-camera simulations had tie point image observation precisions of 0.6 and 0.5 pixels, respectively. Each row represents the results of one bundle adjustment of a simulated image network in VMS. All camera parameters were fixed at zero unless indicated otherwise; values in italics were invariant within the adjustment

Estimated camera parameters	Doming amplitude (mm)	Un-modelled mean camera position error (forwards, mm)	C_y (pixels)	$K_1 \times 10^{-7}$	$P_2 \times 10^{-7}$	Camera parameter correlations	
						$P_2: C_y$	$P_2: K_1$
All fixed	0.4 ± 1.2	0.1 ± 2.7	0.0	0.0	0.0		
K_1	-129.0 ± 9.6	-0.4 ± 8.5	0.0	104.8 ± 7.8	0.0		
Fixed P_2 error	0.4 ± 3.5	-20.4 ± 4.3	0.0	0.0	100.0		
C_y , fixed P_2 error	0.5 ± 3.7	2.9 ± 2.9	2.06 ± 0.54	0.0	100.0		
P_2	0.4 ± 1.2	0.0 ± 2.7	0.0	0.0	0.4 ± 3.5		
P_2, C_y	0.5 ± 1.2	2.7 ± 2.8	0.24 ± 0.54	0.0	0.6 ± 3.6	0.12	
Nadir camera P_2, C_y, K_1	-129.0 ± 9.5	2.4 ± 8.5	0.22 ± 0.54	104.8 ± 7.8	-0.8 ± 3.6	0.04	-0.03
All fixed	0.0 ± 1.1	-0.2 ± 2.1	0.0	0.0	0.0		
K_1	-5.7 ± 1.2	1.6 ± 2.0	0.0	4.9 ± 1.6	0.0		
Fixed P_2 error	-6.0 ± 2.7	-17.7 ± 3.8	0.0	0.0	100.0		
C_y , fixed P_2 error	-4.7 ± 3.2	-1.0 ± 2.0	1.58 ± 0.12	0.0	100.0		
P_2	0.1 ± 1.1	0.1 ± 2.1	0.0	0.0	-1.3 ± 2.8		
Inclined camera (5° pitch) P_2, C_y	0.0 ± 1.1	-1.5 ± 2.1	-0.18 ± 0.12	0.0	-3.0 ± 3.0	0.41	
P_2, C_y, K_1	-57.5 ± 4.4	15.2 ± 5.1	1.20 ± 0.22	46.5 ± 5.9	81.6 ± 11.2	0.84	0.96

symbols). Direct interaction between the estimated decentring distortion and camera inclination was underscored by individually freeing the different decentring parameters, P_1 and P_2 . For a camera oriented off-nadir in pitch (i.e. rotating a camera forward or backward around the image x -axis), doming mitigation was only compromised if P_2 (giving unidirectional corrections in the y -direction, Figure 2) was free to adjust (Figure 6b). If a camera was off-nadir in roll (i.e. rotated left or right around the y -axis), then freeing P_2 had no detectable influence, but enabling optimization of P_1 (giving unidirectional corrections in the x -direction, Figure 2) compromised doming mitigation (Figure 6c). Thus, correlations between radial and decentring camera parameters become interdependent with camera look angle and, hence, remove the advantage of the convergent geometry. Whilst P_1 and P_2 terms are used together to describe characteristic decentring distortion within the Brown–Conrady model, for simplicity, our subsequent analysis of decentring and systematic topographic error focused on camera pitch and, thus, on P_2 .

For further insight into the processes linking decentring distortion and topographic doming error we also analysed error in estimated camera position and principal point coordinate. In all scenarios that demonstrated topographic doming, estimated camera positions were associated with a related upward systematic doming error, and with radially oriented horizontal error that increased in magnitude with distance from the centre of the image network coverage (Figure 7a, b). Modelling (using Equations 3 and 4) and then removing such systematic error components of camera orientation enabled the non-dome-geometry error components to be observed (Figure 7c). For surveys with a nadir camera, Equations 3 and 4 appeared to describe all of the systematic effects, to leave reasonably randomly distributed un-modelled residual errors (Figure 7c, d, left panels). However, for a 5° pitched camera, model residuals showed remaining systematics in horizontal position error, representing a mean forward displacement of ~15 mm (Figure 7c, d, right panels). Thus, when including decentring in the bundle adjustment, the reduction in doming mitigation by camera inclination was associated with a systematic forward-directed component of camera position error, as well as error in K_1 and P_2 estimates (Table 2).

Simulations in which different distortion parameters were held fixed in the bundle adjustment clarified the relationships involved (Table 2). For surveys with a nadir camera and with radial distortion parameters fixed and error-free, a fixed decentring error did not result in detectable topographic doming because it could be compensated for by either displacement of the estimated camera positions or, preferentially, by offset in the estimated principal point position, C_y (Table 2). With an inclined camera, the same compensation mechanisms operated but were less effective, and small but detectable topographic doming was present. However, if the K_1 radial distortion parameter was also estimated in the bundle adjustment then topographic doming developed and was associated with error in K_1 , C_y and P_2 , as well as with systematic forward offsets in camera position. Thus, correlation between the estimated parameters (with magnitudes > 0.8, Table 2) effectively enabled the doming mitigation effect of camera inclination to be counteracted through error propagation between estimated radial and decentring distortion. Note that the resulting doming amplitude was more than an order of magnitude greater than when decentring was held fixed with a larger error (Table 2), i.e. error in decentring distortion alone had minimal effect on topographic error in the double-grid survey style simulated image networks.

Survey sensitivity to systematic error

Processing any individual simulation instance in PhotoScan gave results that were approximately equally likely to present either dishing or doming systematic error (as represented by either a negative or a positive ‘doming amplitude’ value respectively). This contrasts with the single-sign doming results from VMS and probably reflects differences in the numerical bundle adjustment schemes in the different applications. Consequently, processing repeated simulations of any one survey design in PhotoScan generated a distribution of doming amplitudes apparently symmetric about zero (Figure 8). For such distributions, a mean value would not usefully describe the survey susceptibility to systematic error, so we use the standard deviation to characterize the potential magnitude of doming error for any particular survey design.

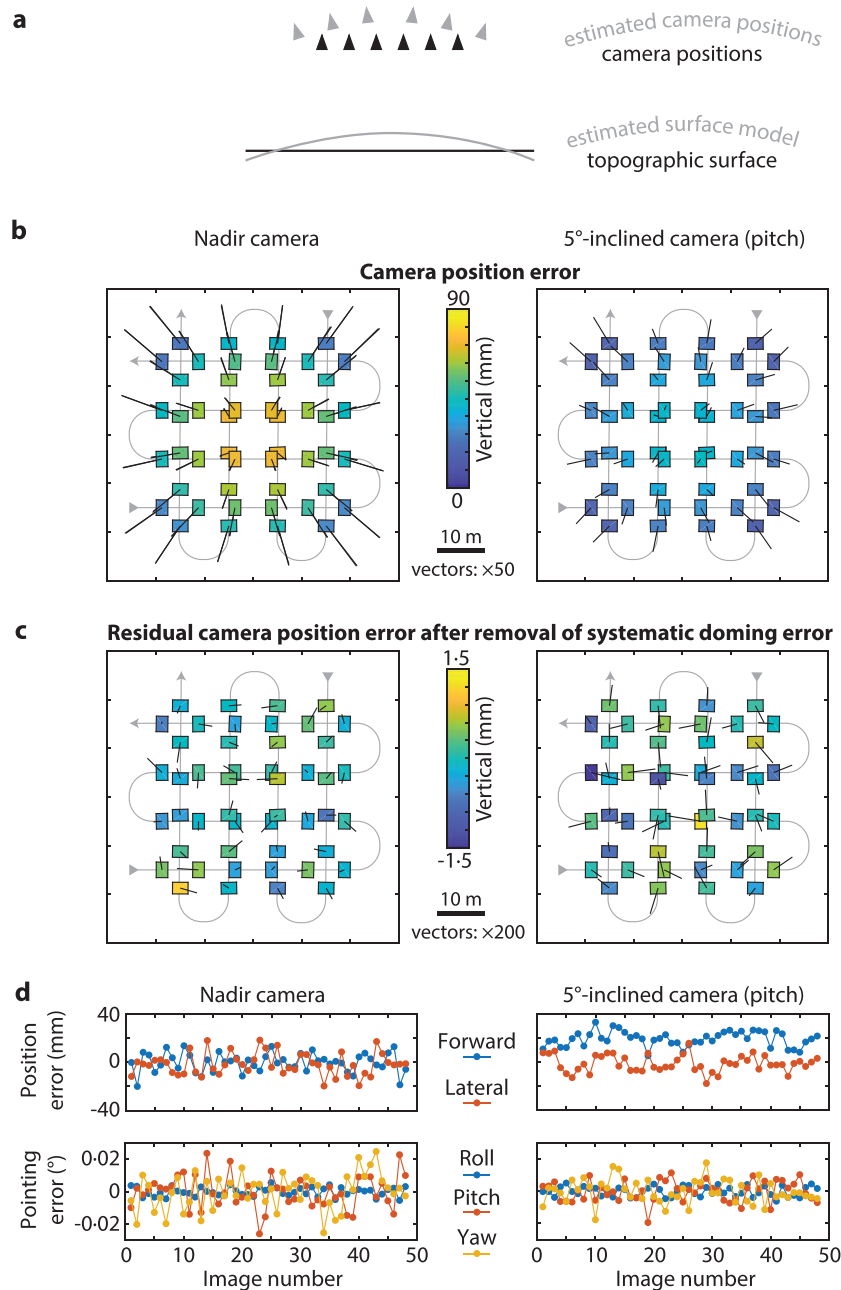


FIGURE 7. Systematic error in camera orientation estimates, for simulated surveys carried out for either a nadir camera or an inclined camera (5° forward pitch), and processed with VMS. The presented results represent the averages of five simulations. The nadir- and inclined-camera simulations had tie point image observation precisions of 0.6 and 0.5 pixels, respectively, and had topographic doming amplitudes of ~130 and ~70 mm. Correlations between camera parameters K_1 , C_y and P_2 had magnitudes < 0.06 for nadir-camera simulations and > 0.77 for inclined-camera simulations. (a) Schematic cross-section illustration of the systematic displacements in estimated camera positions and orientation associated with surface doming error. (b) Plan view of camera position error for surveys with a nadir or inclined camera. Camera positions are illustrated by the rectangles, with vertical and horizontal error given by colour and black vectors respectively. The simulated flight paths are shown by the underlying grey arrows. (c, d) Residual camera orientation error after modelling and removing systematic doming (Equations 3 and 4), showing a mean forward horizontal displacement of the inclined camera [shown by alignment of the black vectors in the right panel of (c) and the ~20 mm ‘forward’ offset in the top right panel of (d)]. [Colour figure can be viewed at wileyonlinelibrary.com]

The PhotoScan results showed the same broad relationships as observed in the VMS-processed simulations between doming amplitude, camera inclination and distortion parameters. For example, with P_2 estimated within bundle adjustments, simulations based on either a nadir camera or a camera inclined 5° in pitch showed similar distributions of dome amplitudes (i.e. the estimated decentring parameter minimized any doming mitigation from camera inclination, Figure 8a), with dome amplitude correlated with K_1 (Figure 8b). The P_2 values were well correlated with dome amplitude and K_1 values for inclined camera surveys, but were essentially uncorrelated for nadir cameras (Figure 8c, d).

Comparing survey susceptibility to systematic error for different survey design characteristics showed the following.

Camera inclination

For camera-nadir surveys, whether or not P_2 was free within the bundle adjustment had little effect on systematic error in the results (Figure 9, first column, comparing results from camera models ‘All parameters’ and ‘All except P_2 ’). Larger differences between results reflected the total number of estimated camera model parameters (compare black with grey symbols); as anticipated, likely doming amplitudes increased with increasing numbers of estimated parameters. However, for surveys with

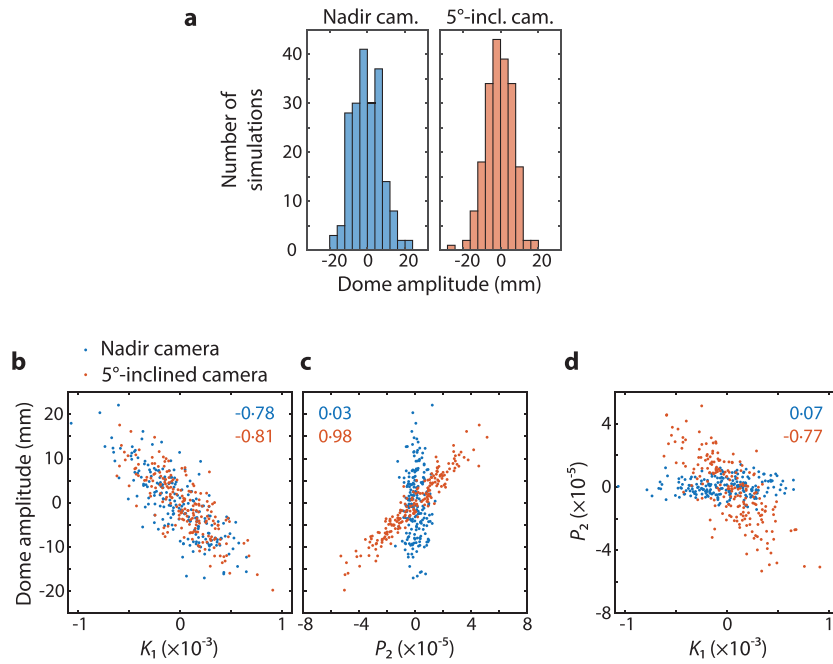


FIGURE 8. Distributions of doming amplitude and associated camera parameter values from survey simulations (Table 1) processed in PhotoScan, with P_2 estimated. Surveys used either a nadir-pointing camera (blue) or a camera inclined at 5° (red) in pitch. Distributions of doming amplitude (a), and correlations between (b) doming amplitude and K_1 , (c) doming amplitude and P_2 , and (d) between K_1 and P_2 values. [Colour figure can be viewed at wileyonlinelibrary.com]

non-zero mean camera inclinations (Figure 9, three right-most columns), estimating P_2 could strongly compromise doming mitigation, particularly in camera models with many other estimated parameters.

Random perturbations from nominal camera directions

Increasing the random perturbation of camera directions reduced doming error (Figure 9a), and this effect was greatest when using a nadir-pointing camera (Figure 9a, 0°). However, with an inclined camera, doming was already effectively mitigated by the camera inclination, unless P_2 was estimated (Figure 9a, $5\text{--}15^\circ$). If P_2 was estimated, then random perturbations in pointing direction with a standard deviation of 3° were sufficient to reduced systematic error to levels close to those obtained if P_2 was held constant.

Precision of tie point image observations

Surveys with poorer quality tie point image observations (i.e. with larger image residuals) had increased likelihood of generating surface models with detectable doming (Figure 9b). This effect was partly mitigated for inclined cameras, but mitigation was weak if P_2 was estimated (Figure 9b, $5\text{--}15^\circ$).

Image overlap

The simulations demonstrated that systematic topographic error was relatively insensitive to variations in image overlap. Substantial reductions in doming were only provided by image overlap increases for nadir surveys with overlaps $< 70\%$, or for surveys with a 5° -inclined camera processed with a full camera model (Figure 9c).

Topographic variability

The effects of different magnitudes of topographic relief, either within images or between images, were similar (Figure 9d, e). As anticipated, a wider range of observation distances (i.e. either surveying rougher terrain or a steeper slope) generally reduced doming, and was particularly effective for nadir surveys (Figure 9d, e; 0°). However, for surveys with an inclined camera, substantial improvements due to increased

topographic relief were only seen if doming mitigation by camera inclination was compromised by P_2 being estimated.

Field surveys

The field surveys (Table 3) were carried out successfully under relatively calm, sunny conditions with intermittent cloud. Processing the image sets was straightforward, with only a few images requiring removal from peripheral regions of the surveys due to weak matching. Such images were identified through having < 1000 or poorly distributed tie points, resulting from either the presence of trees (la Borgne d'Arolla) or extreme scale changes (Tsijiore Nouve; see Table Table S1).

Without GCPs in the bundle adjustment, most surveys showed significant ($p < 0.05$) doming, but doming amplitude was greatest by almost an order of magnitude within the Borgne d'Arolla surveys carried out with an inclined camera (Figures 10, 11). In line with the simulation results (e.g. Figure 6), these inclined-camera surveys also demonstrated the strongest correlations between P_2 and K_1 distortion parameters (Figure 11, red circles). The magnitude of the decentring corrections were similar for all surveys (giving maximums of ~ 3 to 4 pixels), with radial corrections being ~ 5 or 10 times greater. Considering all Tsijiore Nouve surveys, the maximum radial corrections had a standard deviation of $< 3\%$ but, for la Borgne d'Arolla, they varied by $\sim 18\%$ between the nadir and 10° -inclined camera surveys, in line with the strong differences in observed doming within these surveys (Figures 10a, 11a).

The inclusion of GCPs as control points within the bundle adjustment reduced dome amplitudes, although, with 50% of GCPs retained as independent check points, only nadir surveys of the relatively low-relief topography of la Borgne d'Arolla generated results in which doming became no longer significant (Table 3, Figure 11, unshaded bars). In line with this, the Monte Carlo analyses demonstrated that increasing the number of GCPs as control did not substantially reduce Z-error further for nadir surveys (e.g. Figure 12a, left panel; median $RMSE_Z$

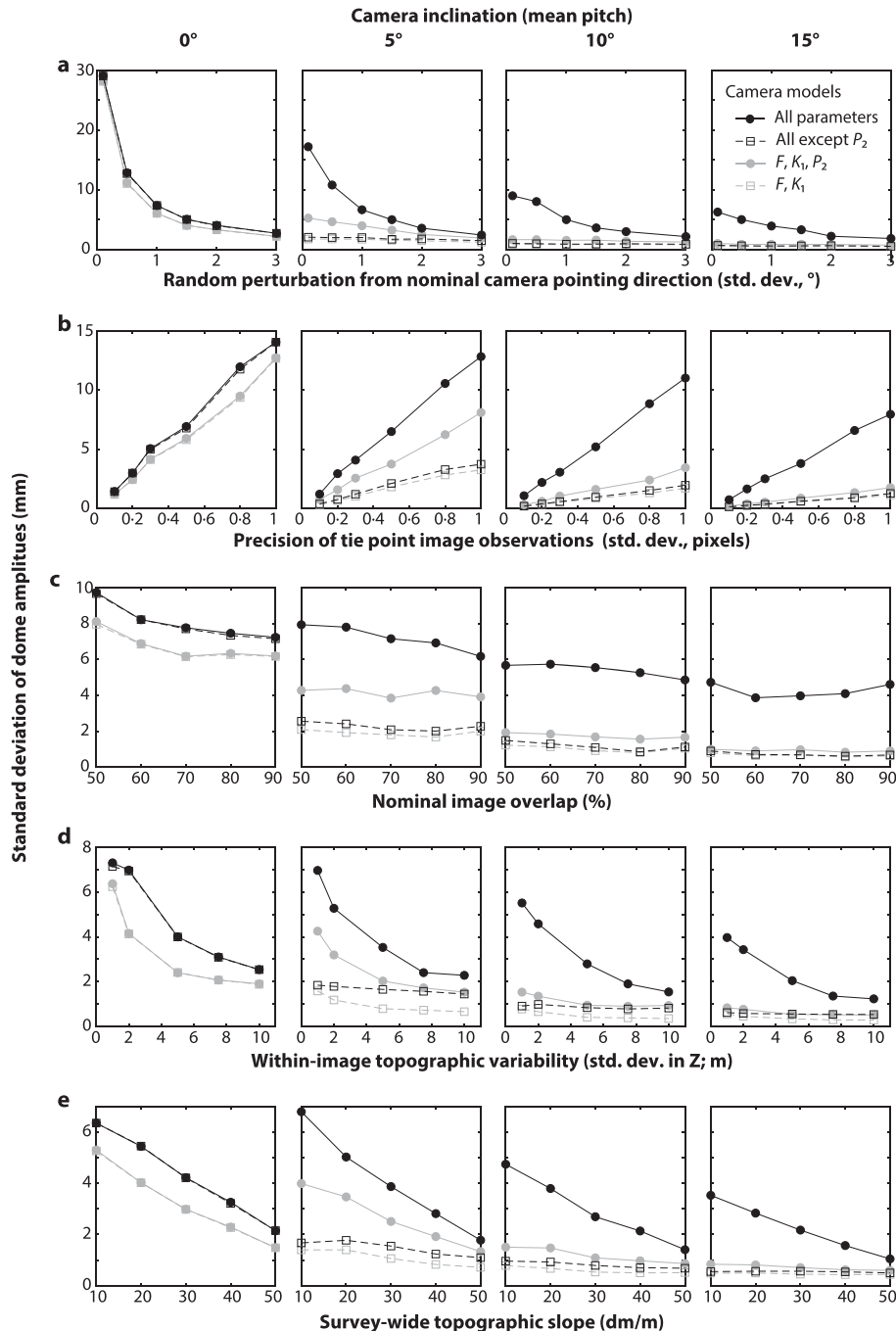


FIGURE 9. Survey sensitivity to topographic doming as a function of (a) the magnitude of random perturbations to camera orientations, (b) the magnitude of tie point image observation precision, (c) image overlap, and topographic variability either (d) over within-image spatial scales, or (e) as a survey-wide slope giving inter-image differences. The columns present results for surveys carried out with cameras at four different inclinations (including nadir), and the symbols (see legend in the top right graph) distinguish four different camera models, with ‘all parameters’ denoting F and $C_x, C_y, B_{1,2}, K_{1-3}, P_{1,2}$ (i.e. as given in Table 1).

values of ~ 13 mm, or 0.8 GSD), indicating that topographic shape was accurately described from the image data alone. In contrast, the tendency for strong doming in inclined-camera surveys of la Borgne d’Arolla resulted in greater $RMSE_Z$ values, and all increases in control helped to reduce error magnitudes (e.g. Figure 12a, right panel, with check point median $RMSE_Z$ values decreasing steadily from 121 mm for 19 control points to 106 mm for 34 control points, 7.9 – 6.9 GSD, respectively). However, with this error comprising both random and modellable systematic (Equation 5) components, it could be reduced consistently to nadir-survey magnitudes by removing the modelled systematic contribution (Figure 12a, right panel, grey symbols). The remaining error (~ 13 mm, or ~ 0.8 GSD) was almost independent of the number of GCPs used for control,

and was a magnitude consistent with the precision of the total station ground survey measurements of the GCP coordinates. Such agreement indicates that the dominant accuracy issues had been successfully accounted for by the modelling, to leave residual error in line with expected precision magnitudes.

The steep topography of Tsjiore Nouve resulted in smaller overall systematic error in inclined-camera surveys than for la Borgne d’Arolla (dome amplitudes of < 100 mm, compared with > 300 mm respectively, Figure 11). However, error mitigation through modelling was potentially less effective, and removal of systematic components did not always reduce error on GCPs to the levels achieved in a nadir-camera survey (Figure 12b, Tables 3 and S3). Nevertheless, residual error on GCPs was generally < 1.5 GSD.

Table 3. Summary of the Arolla field surveys and their results

Survey name	Date,	2018 (dd/yy)	Nominal flight height and camera angle (m, deg)	Ground sampling distance, GSD (mm)	Check point RMSE _Z ^a (mm [GSD])		Dense point cloud ^b (mm [GSD])
					After dome correction	Mean Z precision ^c	Mean LoD _{95%} ^d
<i>La Borgne d'Arolla</i>							
30m_00degr_nadir	01/06	30, nadir	7.8	14.9 [1.9]	^e	6.4 [0.8]	31.5 [4.0]
60m_00degr_nadir	01/06	60, nadir	15.6	16.5 [1.1]	14.6 [0.9]	5.3 [0.3]	^f
90m_00degr_nadir	01/06	90, nadir	24.7	23.6 [1.0]	^e	7.4 [0.3]	34.5 [1.4]
60m_10degr_1	30/05	60, 10°	15.6	155.7 [10.0]	13.7 [0.9]	7.0 [0.5]	33.6 [2.2]
60m_10degr_2	01/06	60, 10°	14.9	101.7 [6.8]	14.1 [0.9]	6.9 [0.5]	33.2 [2.2]
60m_10degr_3	01/06	60, 10°	15.3	97.1 [6.3]	13.2 [0.9]	6.7 [0.4]	32.4 [2.1]
<i>Tsijiore Nouve</i>							
60m_00degr_nadir_1	25/07	60, nadir	18.0	10.9 [0.6]	11.0 [0.6]	8.7 [0.5]	41.4 [2.3]
60m_00degr_nadir_2	25/07	60, nadir	17.6	10.8 [0.6]	^e	7.9 [0.4]	^f
60m_00degr_nadir_3	26/07	60, nadir	17.6	31.8 [1.8]	21.7 [1.2]	8.6 [0.5]	41.2 [2.3]
60m_10degr_1	25/07	60, 10°	16.5	23.5 [1.4]	15.8 [1.0]	8.2 [0.5]	40.1 [2.4]
60m_10degr_2	25/07	60, 10°	18.3	13.6 [0.7]	12.7 [0.7]	8.7 [0.5]	41.2 [2.3]
60m_10degr_3	26/07	60, 10°	18.6	26.6 [1.4]	12.0 [0.6]	8.8 [0.5]	41.5 [2.2]

^aFor 50% of ground control points (GCPs) used as check points.

^bFor points within the areas of interest shown in Figures 10 and 14.

^cValues estimated by Metashape bundle adjustment.

^dM3C2-PM results determined using an effective precision multiplier, $k = 2$, and, where converted to ground sampling distance (GSD), done so using the GSD of the non-reference survey.

^eNo significant ($p \geq 0.05$) doming detected.

^fUsed as the best-case reference survey against which other surveys were compared.

For inter-survey comparisons between full topographic data sets (dense point clouds), the 60-m nadir survey of la Borgne d'Arolla, and the nadir survey of Tsijiore Nouve that showed the smallest dome amplitude (60m_00degr_nadir_2; Figure 11, Table S1) were reprocessed with all GCPs used as control, and used as the best-case reference surveys. All other surveys, except the remaining nadir surveys of la Borgne d'Arolla, had significant ($p < 0.05$) systematic error that could be modelled and removed (Table S3). The Metashape-derived point coordinate precisions (interpolated over the dense point clouds) had mean values in Z of ~5 to 7 mm (0.3–0.8 GSD) for la Borgne d'Arolla and ~8–9 mm (0.4–0.5 GSD) for Tsijiore Nouve – values that are approximately half those of the RMSE_Z on check points (Table 3, cf. Table S4). In line with this, M3C2-PM comparisons between nadir-camera surveys showed that > 95% of points lay within LoD_{95%} of their reference survey for an effective precision multiplier, k , of ~2 (Figure 13), i.e. the dense point clouds met expected repeatability statistics if effective point coordinate precisions were assumed to be approximately twice as large as those estimated within the Metashape bundle adjustment.

For the strongly domed, inclined-camera surveys of la Borgne d'Arolla that were carried out on the same day as the reference survey, only 60–70% of points were within LoD_{95%} of the reference survey data, even for $k = 5$ (i.e. an effective precision of 5σ ; Figure 13a), reflecting the substantial accuracy issues. Nevertheless, after topographic correction for systematic doming (Equation 5), the processed results satisfied the LoD_{95%} criterion for k values of ~2.0 and 2.3 (Figure 13a). For the Tsijiore Nouve surveys, the much smaller correction involved led to much smaller magnitude improvements, but all surveys satisfied the LoD_{95%} criterion for $1.1 < k < 2.4$ (Figure 13b).

Such cumulative summaries do not expose spatial patterns, and correction of la Borgne d'Arolla topography enabled comparison of surveys from either side of a rainfall event to reveal

realistic geomorphic change detection, even from an initially strongly domed dataset (Figure 14a). However, some clear artificial distribution of residual error in the Tsijiore Nouve results (Figure 14b) suggested that, whilst systematic error magnitude was smaller than for the lower-relief topography of la Borgne d'Arolla, the distribution could be more complex for the higher-relief topography and, thus, less fully captured by the straightforward doming correction.

Discussion

Our combined simulation and field-based approach provides a generalized insight into factors affecting the accuracy of UAV-photogrammetry topographic surveys, and is particularly relevant for the accessible UAV systems used widely in geomorphic research. Accuracy issues result from the relatively weak image network geometry of the 'double-grid' flight plan strategies that represent the standard provision in flight planning software for topographic survey. The subsequent topographic correction method demonstrated successful reduction of systematic error in real UAV survey results, and enables the wider use of spatially-variable precision estimates for uncertainty-bounded change detection in geomorphic applications.

Decentering lens distortion

The growing trend of cameras applying generic manufacturer-derived on-board image corrections requires changes, and caution, in our expectations for lens distortion modelling in subsequent processing. For such imagery, distortion models derived during photogrammetric analyses will represent corrections to the initially applied corrections. Given that manufacturers' corrections largely aim to reduce radial

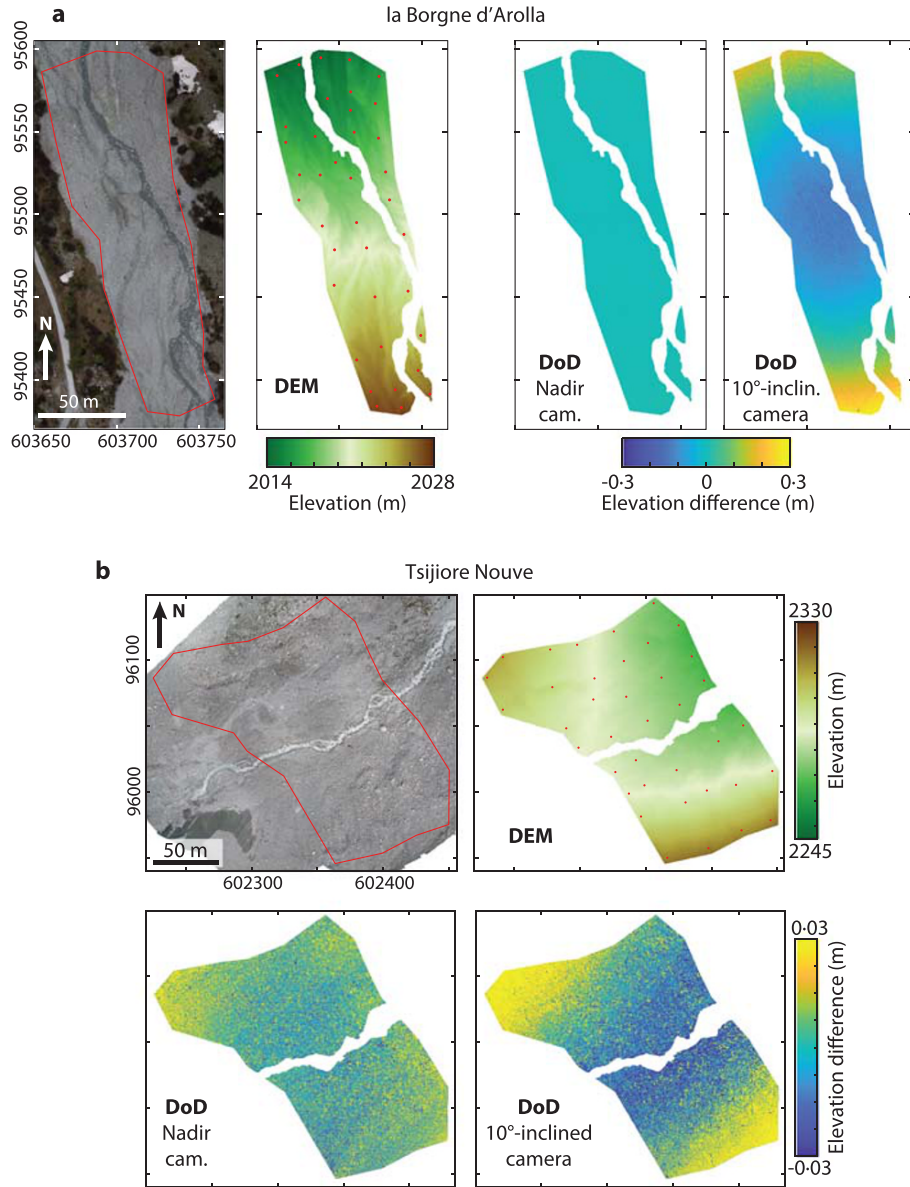


FIGURE 10. Systematic vertical error in digital elevation models (DEMs) for (a) relatively low-relief topography of la Borgne d'Arolla and (b) the steep moraines of Tsijiore Nouve. Both panels show a reference survey orthomosaic (left) with the area analysed outlined in red (coordinates are in CH1903/LV03), and the associated DEM with GCPs indicated by red circles. The DEMs have been cropped to remove areas of water surface. The DEMs of difference (DoDs) show vertical differences between the reference DEMs and those derived using GCPs only for scaling and orienting the results (i.e. not within the bundle adjustment). Note that DoD colour scale for (a) la Borgne d'Arolla covers an order of magnitude larger values than that for (b) Tsijiore Nouve. [Colour figure can be viewed at wileyonlinelibrary.com]

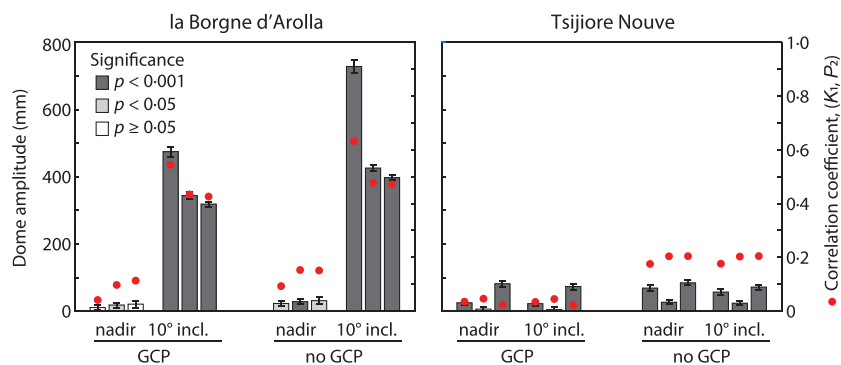


FIGURE 11. Systematic error magnitudes and correlation between the K_1 and P_2 lens distortion parameters for surveys of la Borgne d'Arolla and Tsijiore Nouve. Surveys were carried out with an inclined or nadir camera, and processed with or without GCPs included in the bundle adjustment. Bars represent the modelled systematic error on GCPs (Equation 5) as the amplitude of the 'doming' error component at a distance of 120 m from the survey centre. The bars are shaded by the significance of the associated doming parameter, d , in Equation 5 (i.e. dark grey indicating highly significant; $p < 0.001$). Note that $p \geq 0.05$ for the bars that are too small for visible shading. [Colour figure can be viewed at wileyonlinelibrary.com]

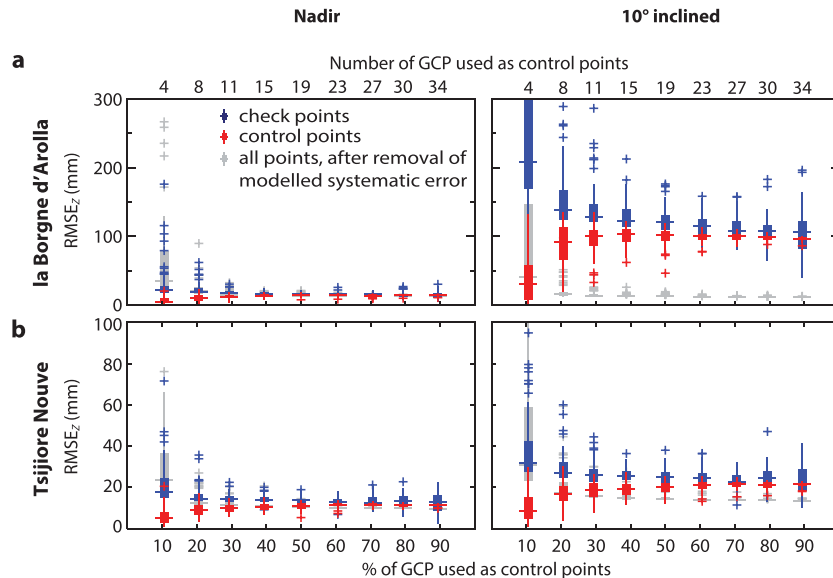


FIGURE 12. The influence of ground control on surveys of (a) la Borgne d'Arolla and (b) Tsjiore Nouvelle, carried out with a nadir camera (left column) and an inclined camera (right column). Within the box plots, each distribution represents the Z-component of error on GCPs from 200 self-calibrating bundle adjustments, with each adjustment using a specific number of randomly selected GCPs as control points. Horizontal bars indicate the median root mean square Z-error ($RMSE_z$) values, with boxes extending between the 25th and 75th percentiles and whiskers denoting the full range of the results not considered outliers (shown by + symbols). Grey symbols show the results following subtraction of systematic error that had been modelled from the control-GCPs only. The analyses shown are for surveys (a) 60m_00degr_nadir and 60m_10degr_3, and (b) 60m_00degr_nadir_1 and 60m_10degr_1 (Table 3). [Colour figure can be viewed at wileyonlinelibrary.com]

distortion, they are likely to alter the relative importance of decentring distortion since the centre of the practical radial distortion may not coincide with the centre of the image format. Existing recommendations to store and process images in raw format avoid such issues, and are suited to the physically-based lens distortion models integrated into most SfM-photogrammetry software (e.g. Mosbrucker et al., 2017; O'Connor et al., 2017). However, raw format is not usually recorded by default in widely available consumer-grade systems, is not always supported by SfM-based software, and is associated with image file sizes that are typically much larger than pre-processed JPEG-format image output (e.g. the image in Figure 1a is ~40 Mb in raw DNG format and ~8 Mb as JPEG). To the authors' knowledge, the use of raw format or alternative distortion models [e.g. the multiple, stacked model available in MicMac (Tournadre et al., 2015), or see Reznicek and Luhmann (2019) for a review] is not currently widespread in geomorphic research, although raw format is standard practice in engineering photogrammetry and heritage recording

(MacDonald et al., 2019) where the capture of critical colour information is also dependant on raw image processing.

Importantly, our results show that decentring error itself does not generally result in substantial systematic topographic error (Table 2) because it can be compensated by error propagation into estimated camera positions. Only when camera inclination enables correlated error within the radial distortion parameters, does substantial systematic topographic error appear.

Survey sensitivity to topographic doming error

Our simulations enabled isolation and testing of individual factors among the wide range of influencing variables affecting survey error, and highlight the impact of the complex parameter interactions that can develop within photogrammetric processing. In previous work that explored only radial distortion, doming was showed to be mitigated effectively using a gently inclined camera (e.g. 5°, figure 3b of James and

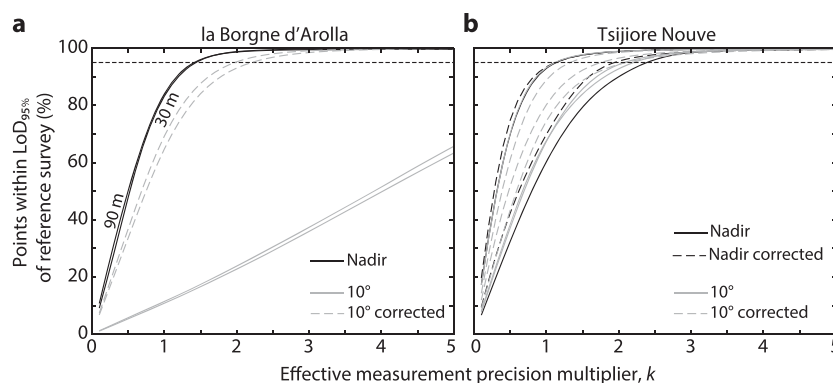


FIGURE 13. The effective precision and increased measurement repeatability through modelling systematic error for (a) la Borgne d'Arolla and (b) Tsjiore Nouvelle surveys. Each curve represents the results of M3C2-PM comparisons between a survey (of specified camera orientation) and its relevant reference survey, for different values of the effective precision multiplier, k (Equation 6). 'Corrected' surveys (dashed lines) represent surveys that have had modelled systematic error (Equation 5) subtracted from the point clouds.

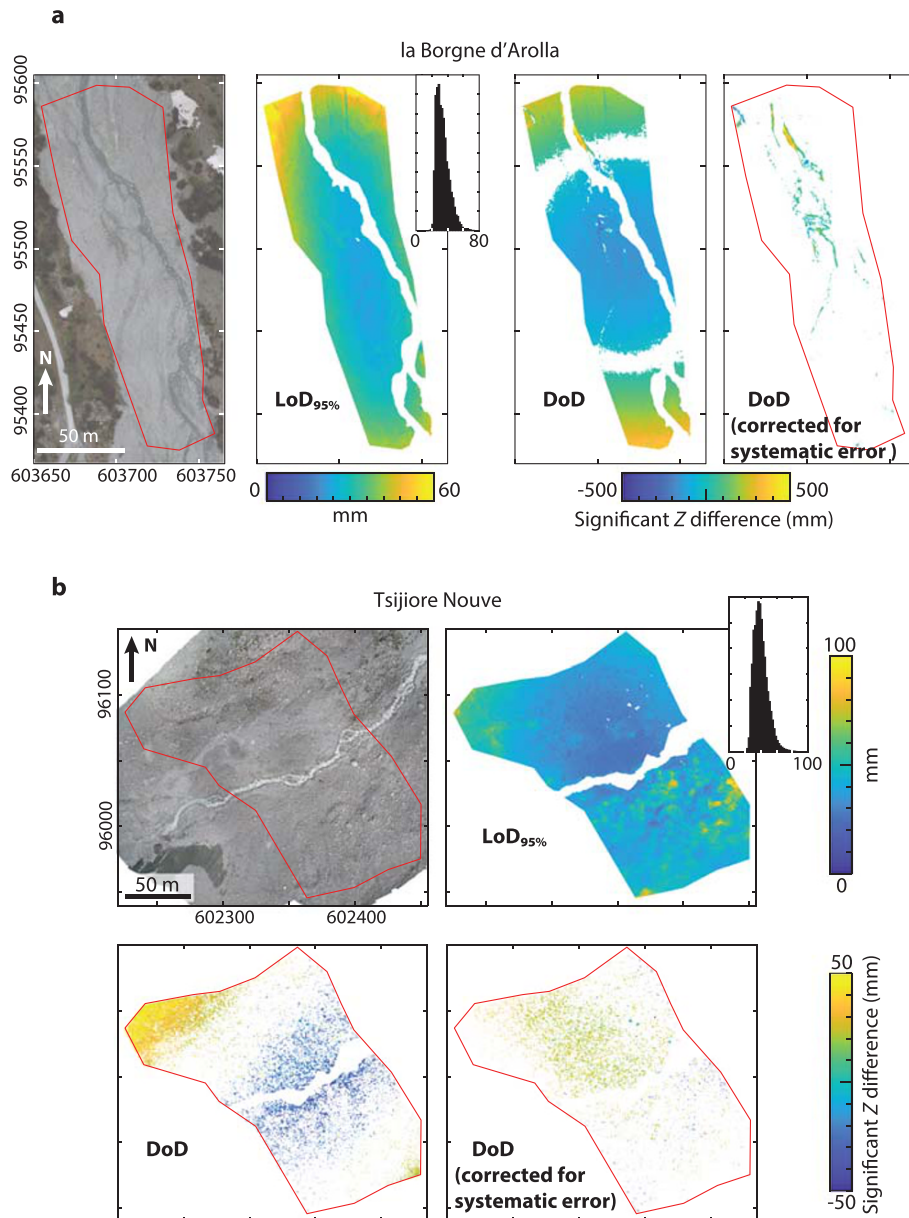


FIGURE 14. Enhanced digital elevation model (DEM) comparisons through removing systematic topographic error and using Metashape precision estimates to determine spatially variable levels of detection. For both (a) la Borgne d'Arolla and (b) Tsijiore Nouve, the upper left panels outline the analysed areas (as in Figure 10) and comparisons are shown between the reference DEMs and surveys carried out with a 10°-inclined camera. The level of detection (given in both map and histogram form) indicates the detectable magnitude of change between each survey pair at the 95% confidence level where the effective measurement precision is assumed to be 2σ (see Figure 13). Within the DEMs of difference (DoDs), white denotes excluded regions (either outside the area of interest, or underwater), or areas where difference magnitude is smaller than the $LoD_{95\%}$ value. [Colour figure can be viewed at wileyonlinelibrary.com]

Robson, 2014a). This remains true (Table 2); however if, as commonly is the case, decentring parameters are also included in the bundle adjustment, then mitigation through camera inclination is compromised (Figure 6). This likely explains elevated errors reported for small camera inclinations (e.g. $< 15^\circ$) in UAV surveys of high-relief landscapes (Nesbit and Hugenholtz, 2019), and underscores the importance of checking for parameter correlations in lens distortion models. Consequently, recommendations to use a gently inclined camera should be limited to cases in which only radial distortion needs to be considered, and should not be applied when a more complex camera model is required, as with many low-cost UAVs (e.g. the Phantom DJI family of quadcopters). Nevertheless, increasing the camera inclination (values of up to 15° are shown in Figure 9) does reduce the effect of radial and decentring parameter interactions and the

magnitude of likely systematic topographic error. This is in line with published field results that have demonstrated the benefit of including oblique images within a nadir survey (e.g. up to 45° , Harwin et al., 2015; Nesbit and Hugenholtz, 2019). To support this further, we reprocessed the nadir-and-four-30°-oblique-camera survey of James and Robson (2014a, their figure 5b), additionally enabling principal point and decentring parameters to vary in the bundle adjustment, and the results verified that doming mitigation remained effective. Survey design will vary depending on the UAV and camera used; ideally, preliminary in-field processing would be carried out to indicate whether survey requirements are likely to be met.

Our simulations also demonstrate the doming sensitivity of surveys to a range of factors other than camera inclination (Figure 9). Notably, doming amplitude appears to have a

strong and approximately linear relationship with the image measurement precision of tie point observations; reducing the quality of the tie point observations from a standard deviation of 0.5 pixels to 1.0 pixels led to more than a doubling in the likely dome amplitude (Figure 9b). Thus, image quality not only controls likely matching success but also the quality of the bundle adjustment results themselves, which will in turn influence both matching success and the degree of systematic error in the derived results. Surveys of sites where the quality of tie point observations may be poor (e.g. due to vegetation cover or areas of water) are likely to be more susceptible to systematic error. As expected from established understanding of photogrammetric image network geometry (Fraser, 1996, 2013; Robson, 1992), the increasingly diverse observation distances when surveying topography with greater relief, increased network strength and reduced the expected magnitudes of systematic error (Figure 9d, e). Similar reductions resulted from increasing the perturbations in camera pointing direction (Figure 9a), thus, the natural variability experienced during practical survey conditions may be beneficial to reduce doming error. We note that, although we have tested a selection of factors that may affect systematic error magnitudes (Figure 9), others factors such as camera stability and tie point spatial variability, are also likely to have some influence.

How much ground control is required?

Incorporating control measurements into the bundle adjustment is an established approach for mitigating systematic error (relevant to any photogrammetric survey), with the number, distribution and quality required depending on the survey design requirements and the strength of the image network (e.g. Krauss, 1993). However, given the wide range of factors that affect the potential magnitude of systematic error, care should be taken not to over-generalize recommendations (e.g. by stating 'required' GCP spatial densities) based on a small numbers of surveys, or from surveys of a specific terrain type, with a specific camera and platform (e.g. Aguera-Vega et al., 2017; Martinez-Carricondo et al., 2018; Rangel et al., 2018; Sanz-Ablanedo et al., 2018; Tonkin and Midgley, 2016). To estimate a reliable minimum ground control deployment for a particular accuracy specification would require a comprehensive model of survey performance, along with appropriate estimates for all the factors involved. Alternatively, simulation approaches can be adopted (Dall'Asta et al., 2015; James et al., 2017b) or Monte Carlo-based analysis of previous, similar surveys (James et al., 2017a; Sanz-Ablanedo et al., 2018).

In cases where systematic error is dominantly doming-related, then our approach of topographic error modelling and correction (Figure 4) offers a potential alternative. Accepting the likelihood of non-negligible but correctable doming leads to the possibility of designing minimal GCP deployments aimed at providing sufficient constraints for a topographic error correction model, rather than at initially achieving acceptable accuracy within the photogrammetric bundle adjustment. As an example, for the doming-sensitive survey of la Borgne d'Arolla shown in Figure 12(a), using eight GCPs and topographic correction resulted in error magnitudes of ~20 mm, compared to ~100 mm when 34 GCPs were used, but without topographic correction (Figure 12a). Appropriate GCP distributions should be in line with current recommendations (i.e. well distributed across the survey volume), and number density could be estimated based on survey extents, expected precision, and constraint requirements for modelling error in processed results.

Direct georeferencing

UAVs with real-time kinematic (RTK) GNSS capabilities are becoming widely available and can provide topographic data with centimetric quality through direct georeferencing (using camera position and potentially also orientation data as control measurements; e.g. Benassi et al., 2017; Chiang et al., 2012; Chudley et al., 2019; Cucci et al., 2017; Eling et al., 2015; Forlani et al., 2018; Gabrlík, 2015; Grayson et al., 2018; Hugenholtz et al., 2016; Rehak et al., 2013; Turner et al., 2014). The specific implications of direct georeferencing on mitigating systematic error have not been explored in detail but it has been previously noted that using camera positions as control data can appear more effective at mitigating doming than GCPs (James et al., 2017b). Our results here suggest how this may operate; using camera position observations as control data should reduce the systematic error in estimated camera positions (Figure 7a, b) and, consequently, also in the related topographic point cloud. In our simulated surveys, systematic horizontal components of camera position error were almost an order of magnitude greater (up to ~210 mm in Figure 7b) than vertical components (~25 mm), so horizontal components of the control coordinates are likely to be more important than vertical components for mitigation. This is convenient, given that GNSS observations are generally approximately twice as good in the horizontal as they are in the vertical. However, we note that some problematic correlations may remain. For example, if an inclined camera is used, additional systematic error in estimated camera positions is oriented systematically in the forward flight direction (Figure 7c, d). Such error could therefore couple into lever arm or shutter timing offset parameters if these are included in the bundle adjustment (e.g. Rehak et al., 2013), with outcomes that would require investigation.

Accuracy and precision in topographic surveys

To maximize the use of UAV-based topographic measurements for geomorphic change detection, a strong understanding of both survey accuracy and precision is required in order to minimize measurement artefacts and to identify surface change rigorously. Most of our surveys displayed accuracy issues which were detectable as statistically significant ($p < 0.05$) topographic doming through modelling error on GCPs as a function of R^2 (Equation 5). Removal of this modelled error reduced RMSE_Z on check points by up to an order of magnitude, to ~14 mm, representing 0.8–1.8 GSD. Such values are aligned with the precision of the GNSS and total station measurements used to determine the GCP locations, and thus reflect the achieved precision of the SfM surveys.

One approach to gain insight into survey-wide measurement repeatability is through comparison of repeated surveys during periods of no surface change (e.g. Goetz et al., 2018; Nesbit and Hugenholtz, 2019). However, this is time-consuming and uncertainties remain with how representative the results may be of surveys collected at other times and under potentially different conditions. An alternative approach is to derive precision estimates for individual surveys [either using a Monte Carlo approach (Dall'Asta et al., 2015; James et al., 2017b), or directly from the bundle adjustment, as in this work for SfM-based software, or James et al. (2017b) or Murtiyoso et al. (2018) for other software]. Although this enables estimates for the specific surveys required, through generally being based on theoretical, Gaussian error distributions, the resulting precision estimates may be optimistic.

By using a combination of both of these two approaches, along with the removal of modelled systematic error, we have

demonstrated surveys that meet a priori statistical expectations for rigorous 3D change detection if internally-estimated precision values are approximately doubled before being used to calculate levels of detection. Although optimism within the precision estimates are a likely component of this, spatial variations indicate that, particularly for areas of strong topographic relief such as Tsijiore Nouve, some residual systematics remain. Thus, sites of strong topographic relief (e.g. Nesbit and Hugenholz, 2019; Smith and Vericat, 2015) may be expected to be less susceptible to systematic error than low-relief areas, but the systematics may be more complex and less effectively captured by a straightforward R^2 model for doming correction.

Conclusions

Appropriate error handling is fundamental to topographic analysis in geomorphic research, and underpins rigorous approaches for quantifying surface change with spatially-variable levels of detection ($LoD_{95\%}$). Here, we demonstrate the critical advantages of clearly separating accuracy issues (bias, or systematic error) from random error (describing the measurement precision). For UAV-based SfM-photogrammetry surveys, which are developing into a leading source of topographic data in geomorphology, we quantify survey sensitivities to accuracy issues and identify a potential vulnerability resulting from the emerging trend of on-camera image pre-processing. For our surveys of proglacial areas (covering both low- and high-relief topography, with single-inclination image sets from either nadir or 10° inclination), we demonstrate up to order-of-magnitude error reduction in topographic data through modelling and removing systematic ('doming') components, and show that survey repeatability can successfully meet $LoD_{95\%}$ estimates determined from approximately twice the magnitude of a priori precision estimates from SfM-based software.

With UAV imagery for geomorphic surveys being increasingly captured by cameras that apply on-board geometric image corrections (e.g. Figure 1), users should be aware that, with such pre-processed imagery, the lens distortions modelled by photogrammetric processing software will represent only the residual image distortions that remain after the generic lens geometry corrections applied by the camera manufacturer. Thus, the physically-based lens distortion models integrated in most SfM-photogrammetry software will be no longer representing the physical optics that they were designed to describe, increasing the potential for resulting misfits that may propagate systematic error into topographic results. When using a physically-based lens distortion model, raw (uncorrected) imagery should be collected and processed if possible.

The sensitivity of photogrammetric surveys to systematic error reflect the factors that underpin robust and accurate camera calibration, such as imaging geometry and the quality of tie point observations. Survey design can address some aspects (noting that image overlap appears to be a relatively weak effect, Figure 9c), but others will depend on survey site characteristics. For example, in line with the established understanding that greater 3D tie point occupancy within a survey volume implicitly strengthens photogrammetric image networks, increasing topographic variability within surveys (Figure 9d, e) resulted in reduced susceptibility to systematic error. Poorer image matching (e.g. due to increased vegetation cover or varying illumination conditions) is likely to increase systematic error magnitudes (Figure 9b).

Systematic error in topographic surveys can be reduced through the effective use of GCPs as control measurements within the bundle adjustment, but the sensitivities described

earlier imply that the GCP density and distribution required to achieve a specific survey design accuracy will vary from site to site, and potentially from survey to survey at the same site. Within topographic results, accuracy problems related to doming can be identified by considering the spatial distribution of error on check (preferably) or control points, or through recognizing unexpected correlations between camera model parameters. Our results show how the use of a gentle camera inclination within UAV surveys can promote strong correlation between decentring and radial distortion parameters, which is sufficient to outweigh the advantage of convergence in imaging direction and allow strong doming error to develop for sites of low topographic relief (Figure 6).

Modelling and subtracting systematic error directly from topographic data (Figure 4) can provide up to order-of-magnitude error reductions for surveys of relatively low-relief topography (Figures 13a, 14a). Inter-survey comparisons of such bias-corrected topographic results showed that survey repeatability achieved mean $LoD_{95\%}$ values of 1.4 to 4.0 GSD (~ 30 – 40 mm; Table 3), reflecting effective measurement precision values that were approximately twice those estimated by Metashape bundle adjustments. Surveys of higher-relief topography are likely to be less affected by systematic doming error than for lower-relief areas, but accuracy issues may be expressed in a more complex form, and leave detectable systematics after doming correction (Figure 14b).

Our straightforward approach addresses one of the major sources of accuracy issues in UAV-based SfM-photogrammetry surveys, and is augmented by now widely available spatially variable topographic precision estimates. Critically, our systematic error correction procedure works on topographic data directly, an approach that is well aligned to a geomorphic community familiar with handling such data. We provide example data, a Python script for precision estimate export, a summary workflow and Matlab topographic correction script in the Supporting Information Data S1, Codes S1, S2, Workflows S1, S2. A topographic correction tool, compiled as a Windows application, is also freely available at <http://tinyurl.com/sfmgeoref>. Given these tools, for the most accurate change detection surveys, particularly of low-relief topography, it is always recommended that GCP check points or short GNSS profiles be taken to allow an independent check.

Acknowledgements—The authors gratefully acknowledge funding for this work from the Fondation Herbette, Université de Lausanne.

Conflict of Interest

None. SNL is the Managing Editor of ESPL. As is journal practice, he was blinded from all elements of stages of the reviewing, decision-making and editorial process which was handled by Michael Kirkby.

Data Availability Statement

The data that support the findings of this study are openly available in figshare at <https://doi.org/10.6084/m9.figshare.c.4677293>.

References

Aguera-Vega F, Carvajal-Ramirez F, Martinez-Carricondo P. 2017. Assessment of photogrammetric mapping accuracy based on variation ground control points number using unmanned aerial vehicle.

- Measurement **98**: 221–227. <https://doi.org/10.1016/j.measurement.2016.12.002>
- Benassi F, Dall'Asta E, Diotri F, Forlani G, di Cella UM, Roncella R, Santise M. 2017. Testing accuracy and repeatability of UAV blocks oriented with GNSS-supported aerial triangulation. *Remote Sensing* **9**: 172. <https://doi.org/10.3390/rs9020172>
- Brasington J, Rumsby BT, McVey RA. 2000. Monitoring and modelling morphological change in a braided gravel-bed river using high resolution GPS-based survey. *Earth Surface Processes and Landforms* **25**: 973–990. [https://doi.org/10.1002/10969-9837\(200008\)25:9%3C973::AidEsp111%3E3.0.Co;2Y](https://doi.org/10.1002/10969-9837(200008)25:9%3C973::AidEsp111%3E3.0.Co;2Y)
- Brasington J, Langham J, Rumsby B. 2003. Methodological sensitivity of morphometric estimates of coarse fluvial sediment transport. *Geomorphology* **53**: 299–316. [https://doi.org/10.1016/S0169-555x\(02\)00320-3](https://doi.org/10.1016/S0169-555x(02)00320-3)
- Brown DC. 1966. Decentering distortion of lenses. *Photogrammetric Engineering* **32**: 444–462.
- Brown DC. 1971. Close-range camera calibration. *Photogrammetric Engineering* **37**: 855–866.
- Carbonneau PE, Dietrich JT. 2017. Cost-effective non-metric photogrammetry from consumer-grade sUAS: implications for direct georeferencing of structure from motion photogrammetry. *Earth Surface Processes and Landforms* **42**: 473–486. <https://doi.org/10.1002/esp.4012>
- Chiang K-W, Tsai M-L, Chu D-H. 2012. The development of an UAV borne direct georeferenced photogrammetric platform for ground control point free applications. *Sensors* **12**: 9161–9180. <https://doi.org/10.3390/s120709161>
- Chudley TR, Christoffersen P, Doyle SH, Abellan A, Snooke N. 2019. High accuracy UAV photogrammetry of ice sheet dynamics with no ground control. *The Cryosphere* **13**: 955–968. <https://doi.org/10.5194/tc-13-955-2019>
- Clarke TA, Fryer JG. 1998. The development of camera calibration methods and models. *Photogrammetric Record* **16**: 51–66. <https://doi.org/10.1111/0031-868x.00113>
- Cramer M, Przybilla H-J, Zurhorst A. 2017. UAV cameras: Overview and geometric calibration benchmark. *International Archives of the Photogrammetry, Remote Sensing and Spatial Information Sciences XLII-2(W6)*: 85–92. <https://doi.org/10.5194/isprs-archives-XLII-2-W6-85-2017>
- Cucci DA, Rehak M, Skaloud J. 2017. Bundle adjustment with raw inertial observations in UAV applications. *ISPRS Journal of Photogrammetry and Remote Sensing* **130**: 1–12. <https://doi.org/10.1016/j.isprsjprs.2017.05.008>
- Dall'Asta E, Thoeni K, Santise M, Forlani G, Giacomini A, Roncella R. 2015. Network design and quality checks in automatic orientation of close-range photogrammetric blocks. *Sensors* **15**: 7985–8008. <https://doi.org/10.3390/s150407985>
- Eling C, Wieland M, Hess C, Klingbeil L, Kuhlmann H. 2015. Development and evaluation of a UAV based mapping system for remote sensing and surveying applications. *International Archives of the Photogrammetry, Remote Sensing and Spatial Information Sciences XL-1(W4)*: 233–239. <https://doi.org/10.5194/isprsarchives-XL-1-W4-233-2015>
- Eltner A, Baumgart P, Maas HG, Faust D. 2015. Multi-temporal UAV data for automatic measurement of rill and interrill erosion on loess soil. *Earth Surface Processes and Landforms* **40**: 741–755. <https://doi.org/10.1002/esp.3673>
- Forlani G, Dall'Asta E, Diotri F, di Cella UM, Roncella R, Santise M. 2018. Quality assessment of DSMs produced from UAV flights georeferenced with on-board RTK positioning. *Remote Sensing* **10**: 311. <https://doi.org/10.3390/rs10020311>
- Fraser CS. 1996. Network design. In *Close range photogrammetry and machine vision*, Atkinson KB (ed). Whittles Publishing: Caithness; 256–281.
- Fraser CS. 1997. Digital camera self-calibration. *ISPRS Journal of Photogrammetry and Remote Sensing* **52**: 149–159.
- Fraser C. 2001. Photogrammetric camera component calibration: A review of analytical techniques. In *Calibration and Orientation of Cameras in Computer Vision*, Gruen A, Huang TS (eds). Springer: Berlin; 95–121.
- Fraser CS. 2013. Automatic camera calibration in close range photogrammetry. *Photogrammetric Engineering and Remote Sensing* **79**: 381–388.
- Fryer JG, Brown DC. 1986. Lens distortion for close-range photogrammetry. *Photogrammetric Engineering and Remote Sensing* **52**: 51–58.
- Fryer JG, Mitchell HL. 1987. Radial distortion and close-range stereophotogrammetry. *Australian Journal of Geodesy, Photogrammetry and Surveying* **46**: 123–138.
- Gabrilik P. 2015. The use of direct georeferencing in aerial photogrammetry with micro UAV. *IFAC-PapersOnLine* **48**: 380–385. <https://doi.org/10.1016/j.ifacol.2015.07.064>
- Goetz J, Brenning A, Marcer M, Bodin X. 2018. Modeling the precision of structure-from-motion multi-view stereo digital elevation models from repeated close-range aerial surveys. *Remote Sensing of Environment* **210**: 208–216. <https://doi.org/10.1016/j.rse.2018.03.013>
- Grayson B, Penna NT, Mills JP, Grant DS. 2018. GPS precise point positioning for UAV photogrammetry. *Photogrammetric Record* **33**: 427–447. <https://doi.org/10.1111/phor.12259>
- Gruen A, Beyer HA. 2001. System calibration through self-calibration. In *Calibration and Orientation of Cameras in Computer Vision*, Gruen A, Huang TS (eds). Springer: Berlin; 163–193.
- Harwin S, Lucieer A. 2012. Assessing the accuracy of georeferenced point clouds produced via multi-view stereopsis from unmanned aerial vehicle (UAV) imagery. *Remote Sensing* **4**: 1573–1599. <https://doi.org/10.3390/rs4061573>
- Harwin S, Lucieer A, Osborn J. 2015. The impact of the calibration method on the accuracy of point clouds derived using unmanned aerial vehicle multi-view stereopsis. *Remote Sensing* **7**: 11933–11953. <https://doi.org/10.3390/rs70911933>
- Hastedt H, Luhmann J. 2015. Investigations on the quality of the interior orientation and its impact in object space for UAV photogrammetry. *International Archives of the Photogrammetry, Remote Sensing and Spatial Information Sciences XL-1(W4)*: 321–328. <https://doi.org/10.5194/isprsarchives-XL-1-W4-321-2015>
- Hugenholtz CH, Whitehead K, Brown OW, Barchyn TE, Moorman BJ, Le Clair A, Riddell K, Hamilton T. 2013. Geomorphological mapping with a small unmanned aircraft system (sUAS): Feature detection and accuracy assessment of a photogrammetrically-derived digital terrain model. *Geomorphology* **194**: 16–24. <https://doi.org/10.1016/j.geomorph.2013.03.023>
- Hugenholtz C, Brown O, Walker J, Barchyn T, Nesbit P, Kurcharczyk M, Myshak S. 2016. Spatial accuracy of UAV-derived orthoimagery and topography: Comparing photogrammetric models processed with direct geo-referencing and ground control points. *Geomatica* **70**: 21–30. <https://doi.org/10.5623/cig2016-102>
- James MR, Robson S. 2014a. Mitigating systematic error in topographic models derived from UAV and ground-based image networks. *Earth Surface Processes and Landforms* **39**: 1413–1420. <https://doi.org/10.1002/esp.3609>
- James MR, Robson S. 2014b. Sequential digital elevation models of active lava flows from ground-based stereo time-lapse imagery. *ISPRS Journal of Photogrammetry and Remote Sensing* **97**: 160–170. <https://doi.org/10.1016/j.isprsjprs.2014.08.011>
- James MR, Robson S, Pinkerton H, Ball M. 2006. Oblique photogrammetry with visible and thermal images of active lava flows. *Bulletin of Volcanology* **69**: 105–108. <https://doi.org/10.1007/s00445-006-0062-9>
- James MR, Pinkerton H, Robson S. 2007. Image-based measurement of flux variation in distal regions of active lava flows. *Geochemistry Geophysics Geosystems* **8**: Q03006. <https://doi.org/10.1029/2006GC001448>
- James MR, Robson S, d'Oleire-Oltmanns S, Niethammer U. 2017a. Optimising UAV topographic surveys processed with structure-from-motion: Ground control quality, quantity and bundle adjustment. *Geomorphology* **280**: 51–66. <https://doi.org/10.1016/j.geomorph.2016.11.021>
- James MR, Robson S, Smith MW. 2017b. 3-D uncertainty-based topographic change detection with structure-from-motion photogrammetry: precision maps for ground control and directly georeferenced surveys. *Earth Surface Processes and Landforms* **42**: 1769–1788. <https://doi.org/10.1002/esp.4125>

- KraussK. 1993. *Photogrammetry, Vol. 1: Fundamentals and Standard Processes*. Dümmlers: Bonn.
- KraussK. 2007. *Photogrammetry – Geometry from Images and Laser Scans*. De Gruyter: Berlin.
- LagueD, Brodu N, Leroux J. 2013. Accurate 3D comparison of complex topography with terrestrial laser scanner: Application to the Rangitikei canyon (N-Z). *ISPRS Journal of Photogrammetry and Remote Sensing* **82**: 10–26. <https://doi.org/10.1016/j.isprsjprs.2013.04.009>
- LaneSN, Westaway RM, Hicks DM. 2003. Estimation of erosion and deposition volumes in a large, gravel-bed, braided river using synoptic remote sensing. *Earth Surface Processes and Landforms* **28**: 249–271. <https://doi.org/10.1002/esp.483>
- LuhmannT, Robson S, Kyle S, Boehm J. 2014. *Close-Range Photogrammetry and 3D Imaging*. De Gruyter: Berlin.
- LuhmannT, Fraser C, Maas HG. 2016. Sensor modelling and camera calibration for close-range photogrammetry. *ISPRS Journal of Photogrammetry and Remote Sensing* **115**: 37–46.
- MacDonaldLW, Hosseinineveh A, Robson S. 2019. Photogrammetric analysis of a heritage ceiling. *International Archives of Photogrammetry and Remote Sensing and Spatial Information Sciences XL-5*: 379–383. <https://doi.org/10.5194/isprsarchives-XL-5-379-2014>
- Martinez-CarricondoP, Aguera-Vega F, Carvajal-Ramirez F, Mesas-Carrascosa FJ, Garcia-Ferrer A, Perez-Porras FJ. 2018. Assessment of UAV-photogrammetric mapping accuracy based on variation of ground control points. *International Journal of Applied Earth Observation and Geoinformation* **72**: 1–10. <https://doi.org/10.1016/j.jag.2018.05.015>
- MosbruckerAR, Major JJ, Spicer KR, Pitlick J. 2017. Camera system considerations for geomorphic applications of SfM photogrammetry. *Earth Surface Processes and Landforms* **42**: 969–986. <https://doi.org/10.1002/esp.4066>
- MurtiyosoA, Grussenmeyer P, Börlin N, Vandermeersch J, Freville T. 2018. Open source and independent methods for bundle adjustment assessment in close-range UAV photogrammetry. *Drones* **2**: 3. <https://doi.org/10.3390/drones2010003>
- NesbitPR, Hugenholtz CH. 2019. Enhancing UAV–SfM 3D model accuracy in high-relief landscapes by incorporating oblique images. *Remote Sensing* **11**: 239. <https://doi.org/10.3390/rs11030239>
- NiethammerU, Rothmund S, James MR, Travelletti J, Joswig M. 2010. UAV-based remote sensing of landslides. *International Archives of Photogrammetry, Remote Sensing, and Spatial Information Sciences XXXVIII(Part 5)*: 496–501.
- O'ConnorJ, Smith M, James MR. 2017. Cameras and settings for aerial surveys in the geosciences: Optimising image data. *Progress In Physical Geography* **41**: 325–344. <https://doi.org/10.1177/0309133317703092>
- OuedraogoMM, Degre A, Debouche C, Lisein J. 2014. The evaluation of unmanned aerial system-based photogrammetry and terrestrial laser scanning to generate DEMs of agricultural watersheds. *Geomorphology* **214**: 339–355. <https://doi.org/10.1016/j.geomorph.2014.02.016>
- PeppamV, Hall J, Goodyear J, Mills JP. 2019. Photogrammetric assessment and comparison of DJI Phantom 4 Pro and Phantom 4 RTL small unmanned aircraft systems. *International Archives of the Photogrammetry, Remote Sensing and Spatial Information Sciences XLII-2 (W13)*: 503–509. <https://doi.org/10.5194/isprs-archives-XLII-2-W13-503-2019>
- RangelJMG, Goncalves GR, Perez JA. 2018. The impact of number and spatial distribution of GCPs on the positional accuracy of geospatial products derived from low-cost UASs. *International Journal of Remote Sensing* **39**: 7154–7171. <https://doi.org/10.1080/01431161.2018.1515508>
- RehakM, Mabillard R, Skaloud J. 2013. A micro-UAV with the capability of direct georeferencing. *International Archives of the Photogrammetry, Remote Sensing and Spatial Information Sciences XL-1(W2)*: 317–323.
- ReznicekJ, Luhmann T. 2019. Finite-element approach to camera modelling and calibration. *PFG – Journal of Photogrammetry Remote Sensing and Geoinformation Science* **87**: 1–17. <https://doi.org/10.1007/s41064-019-00068-x>
- RobsonS. 1992. Film deformation in non metric cameras under weak geometric conditions – an uncorrected disaster? *International Archives of Photogrammetry and Remote Sensing* **29**: 561–567.
- RobsonS, Shortis MR. 1998. Practical influences of geometric and radiometric image quality provided by different digital camera systems. *Photogrammetric Record* **16**: 225–248.
- RobsonS, Shortis MR, Ray SF. 1999. Vision metrology with super wide angle and fisheye optics. In *Videometrics VI, Volume 3641*. SPIE: San Jose, CA; 199–206.
- RosnellT, Honkavaara E. 2012. Point cloud generation from aerial image data acquired by a quadcopter type micro unmanned aerial vehicle and a digital still camera. *Sensors* **12**: 453–480. <https://doi.org/10.3390/s120100453>
- Sanz-AblanedoE, Chandler JH, Rodriguez-Perez JR, Ordóñez C. 2018. Accuracy of unmanned aerial vehicle (UAV) and SfM photogrammetry survey as a function of the number and location of ground control points used. *Remote Sensing* **10**: 1606. <https://doi.org/10.3390/rs10101606>
- SmithMW, Vericat D. 2015. From experimental plots to experimental landscapes: topography, erosion and deposition in sub-humid badlands from Structure-from-Motion photogrammetry. *Earth Surface Processes and Landforms* **40**: 1656–1671. <https://doi.org/10.1002/esp.3747>
- TonkinTN, Midgley NG. 2016. Ground-control networks for image based surface reconstruction: An investigation of optimum survey designs using UAV derived imagery and structure-from-motion photogrammetry. *Remote Sensing* **8**: 786. <https://doi.org/10.3390/rs8090786>
- TournadreV, Pierrot-Deseilligny M, Faure PH. 2015. UAV linear photogrammetry. *The International Archives of the Photogrammetry, Remote Sensing and Spatial Information Sciences XL-3(W3)*: 327–333. <https://doi.org/10.5194/isprsarchives-XL-3-W3-327-2015>
- TurnerD, Lucieir A, Wallace L. 2014. Direct georeferencing of ultrahigh-resolution UAV imagery. *IEEE Transactions on Geoscience and Remote Sensing* **52**: 2738–2745. <https://doi.org/10.1109/Tgrs.2013.2265295>
- TurnerD, Lucieir A, de Jong SM. 2015. Time series analysis of landslide dynamics using an unmanned aerial vehicle (UAV). *Remote Sensing* **7**: 1736–1757. <https://doi.org/10.3390/rs70201736>
- WackrowR, Chandler JH. 2008. A convergent image configuration for DEM extraction that minimises the systematic effects caused by an inaccurate lens model. *Photogrammetric Record* **23**: 6–18. <https://doi.org/10.1111/j.1477-9730.2008.00467.x>
- WackrowR, Chandler JH. 2011. Minimising systematic error surfaces in digital elevation models using oblique convergent imagery. *Photogrammetric Record* **26**: 16–31. <https://doi.org/10.1111/j.1477-9730.2011.00623.x>
- WoodgetAS, Carbonneau PE, Visser F, Maddock IP. 2015. Quantifying submerged fluvial topography using hyperspatial resolution UAS imagery and structure from motion photogrammetry. *Earth Surface Processes and Landforms* **40**: 47–64. <https://doi.org/10.1002/esp.3613>

Supporting Information

Additional supporting information may be found online in the Supporting Information section at the end of the article.

Table S1. Arolla surveys: survey details.

Table S2. Arolla survey results: cameras and tie points.

Table S3. Arolla survey results: GCPs.

Table S4. Arolla survey results: dense point cloud precision and level of change detection.

Workflow S1. Workflow for correcting systematic error, including the use of the Matlab code below.

Code S1. A compressed folder containing a Matlab script (estimate_doming_and_correct_dense_cloud.m) and ancillary

function for modelling and subtracting doming error from photogrammetric surveys. Step-by-step instructions are provided within the script.

Data S1. A compressed folder containing example data for use with the Matlab code above.

Workflow S2. Instructions for using 'export_point_coordinate_precision.py', and a comparison of VMS and Metashape point coordinate precision estimates.

Code S2. Metashape Python script for exporting sparse point coordinate precision estimates.